Imaginary-time correlation function thermometry: A new, high-accuracy and model-free temperature analysis technique for x-ray Thomson scattering data

Tobias Dornheim, Maximilian P. Böhme, David A. Chapman, et al.
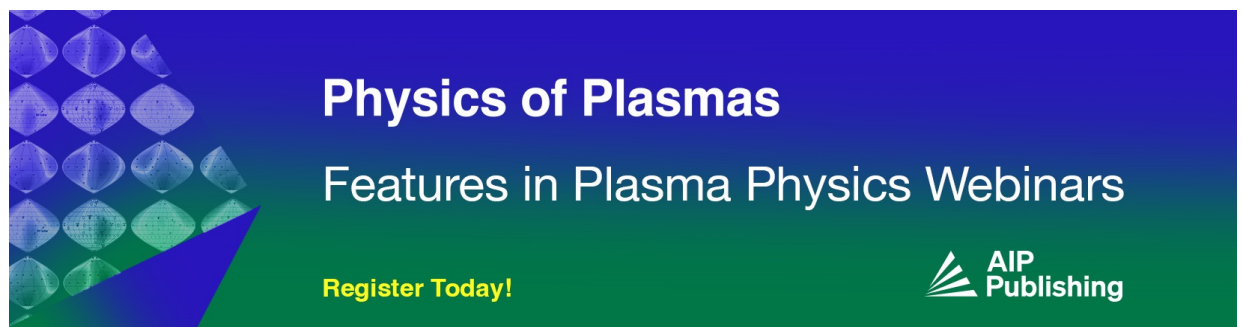
View Online   Export Citation   CrossMark

Physics of Plasmas

Features in Plasma Physics Webinars

Register Today!   AIP Publishing

Imaginary-time correlation function thermometry: A new, high-accuracy and model-free temperature analysis technique for x-ray Thomson scattering data

View Online   Export Citation   CrossMark

Tobias Dornheim,[1,2,a] (iD) Maximilian P. Böhme,[1,2,3] (iD) David A. Chapman,[4] (iD) Dominik Kraus,[2,5] (iD)
Thomas R. Preston,[6] (iD) Zhandos A. Moldabekov,[1,2] (iD) Niclas Schlünzen,[1,2] Attila Cangi,[1,2] (iD)
Tilo Döppner,[7] (iD) and Jan Vorberger[2] (iD)

AFFILIATIONS

[1]Center for Advanced Systems Understanding (CASUS), D-02826 Görlitz, Germany
[2]Helmholtz-Zentrum Dresden-Rossendorf (HZDR), D-01328 Dresden, Germany
[3]Technische Universität Dresden, D-01062 Dresden, Germany
[4]First Light Fusion, Yarnton, Oxfordshire OX5 1QU, United Kingdom
[5]Institut für Physik, Universität Rostock, D-18051 Rostock, Germany
[6]European XFEL, D-22869 Schenefeld, Germany
[7]Lawrence Livermore National Laboratory (LLNL), Livermore, California 94550, USA

[a]Author to whom correspondence should be addressed: t.dornheim@hzdr.de

ABSTRACT

The accurate interpretation of experiments with matter at extreme densities and pressures is a notoriously difficult challenge. In a recent work [Dornheim *et al.*, Nat. Commun. **13**, 7911 (2022)], we have introduced a formally exact methodology that allows extracting the temperature of arbitrary complex materials without any model assumptions or simulations. Here, we provide a more detailed introduction to this approach and analyze the impact of experimental noise on the extracted temperatures. In particular, we extensively apply our method both to synthetic scattering data and to previous experimental measurements over a broad range of temperatures and wave numbers. We expect that our approach will be of high interest to a gamut of applications, including inertial confinement fusion, laboratory astrophysics, and the compilation of highly accurate equation-of-state databases.

I. INTRODUCTION

Over the last few decades, there has been a surge of interest in the properties of matter at extreme conditions.[1] The phase space representing temperatures of $T \sim 10^4$–10^8 K and pressures of $P \sim 1$–10^4 Mbar is called warm dense matter (WDM), which is ubiquitous throughout our universe and occurs in a variety of astrophysical objects such as giant planet interiors[2–6] and brown dwarfs.[7,8] In addition, WDM plays an important role in a number of cutting-edge technological applications. For example, the fuel capsule in an inertial confinement fusion experiment[9,10] traverses the WDM regime on its pathway toward nuclear fusion.[11] Other practical applications include the discovery of novel materials[12–14] and hot-electron chemistry.[15]

In the laboratory, WDM is generated at large research facilities using a number of techniques, see, e.g., the topical overview by Falk.[16] However, the central obstacle is the rigorous interpretation of the experiment because basic parameters such as the temperature cannot be directly measured. In this situation, the x-ray Thomson scattering (XRTS) approach[17] has emerged as a highly useful method. More specifically, it has become common practice to fit an experimentally observed XRTS signal with a theoretical model to infer system parameters such as the temperature.[18–20] Unfortunately, the rigorous theoretical description of WDM is notoriously difficult.[21–23] In practice, however, uncontrolled approximations, such as the artificial decomposition into *bound* and *free* electrons (the cornerstone for Chihara's

famous approach[19,24]), remain widely used. Consequently, the actual interpretation of an experiment might strongly depend on a particular model, which limits the accuracy of equation of state (EoS) tables[20] and other observations.

To overcome this unsatisfactory situation, we have recently introduced a new methodology, referred to as imaginary-time correlation function thermometry (ITCFT),[25] which extracts the temperature from a given XRTS signal directly, without the need for any theoretical models or simulations. In particular, we have proposed to compute the two-sided Laplace transform [Eq. (16)] of the measured intensity, which has a number of key advantages: (1) the impact of the instrument function can be completely removed, without the need for a numerically unstable explicit deconvolution, (2) the method is very robust with respect to noise in the experimental data, and (3) the temperature can be measured for arbitrary complex materials without theoretical constraints. The high practical value of this new approach has been demonstrated in Ref. 25 by reevaluating the XRTS measurements of warm dense beryllium by Glenzer et al.,[26] aluminum by Sperling et al.,[27] and graphite by Kraus et al.[18]

In the present work, we provide a more detailed introduction to the ITCFT method, including a comprehensive discussion of the underlying theoretical framework. In addition, we present an extensive analysis of synthetic XRTS data over a broad range of temperatures and wave numbers. This allows us to clearly delineate the limitations of this approach and to rigorously predict the required experimental specifications to resolve a given plasma temperature. Finally, we systematically investigate the impact of random noise in the experimentally measured intensity and present an empirical procedure for the quantification of the uncertainty in the temperature extracted using ITCFT.

In addition to its direct value as a diagnostic for WDM, we note that the Laplace domain of the dynamic structure factor has a clear physical interpretation as an imaginary-time correlation function.[23,28,29] The latter naturally emerges in Feynman's path integral formulation of statistical mechanics[30,31] and measures the decay of electron–electron correlations along the imaginary-time axis $\tau \in [0, \hbar\beta]$, where $\beta = 1/k_B T$ is the inverse thermal energy. More details on imaginary-time correlation functions have been presented in Refs. 28 and 29. We note that the imaginary-time domain contains the same information as the usual frequency representation. In fact, both representations are complementary and tend to emphasize different aspects of the same information about a given system.[28] Therefore, our approach has the potential to give novel insights beyond the temperature, such as the excitation energy of quasi-particles or physical effects like the exchange–correlation induced alignment of pairs of electrons at metallic densities.[32]

This paper is organized as follows. In Sec. II, we introduce the theoretical basis for the ITCFT technique, including a brief discussion of XRTS (Sec. II B), the extraction of the temperature in the Laplace domain (Sec. II D), its connection to imaginary-time correlation functions,[33,34] and some practical remarks on the convergence with respect to the experimentally observed frequency range (Sec. II E). Section III is devoted to the analysis of synthetic data and is followed by a new framework for the study of the impact of random noise provided in Sec. IV. In Sec. V, we reanalyze the aforementioned experiments by Kraus et al.[18] and Glenzer et al.[26] and, thereby, complement the earlier analysis in Ref. 25 by quantifying the given uncertainties in different properties. The paper is concluded with a summary and an outlook in Sec. VI.

II. THEORY

A. Characteristic parameters and system of units

Unless explicitly specified otherwise, we consider Hartree atomic units (HAU) throughout this paper, i.e., energies, distances, charges, and masses are given in units of the Hartree energy $E_{Ha} = \hbar^2/a_B^2 m_e$, the Bohr radius a_B, the elementary charge e, and the electron mass m_e. From a theoretical perspective, the WDM regime is conveniently characterized by two parameters that are both of the order of unity:[35] (1) the Brueckner parameter $r_s = R_{ee}/a_B$, where $R_{ee} = (3/4\pi n_e)^{1/3}$ and n_e are, respectively, the Wigner–Seitz radius and the number density of the electrons, and (2) the degeneracy parameter $\Theta = k_B T/E_F$ with E_F denoting the Fermi energy. The latter is connected to the Fermi wave number

$$q_F = (3\pi^2 n_e)^{1/3} = \left(\frac{9\pi}{4r_s^3}\right)^{1/3} \quad (1)$$

via $E_F = \hbar^2 q_F^2/2m_e$. The plasma frequency is given by $\omega_{pe} = e^2 n_e/\epsilon_0 m_e$ ($= (3/r_s^3)^{1/2}$ in HAU). For completeness, we note that we restrict ourselves to the fully unpolarized case with the same number of spin-up and spin-down electrons, $n_e^\uparrow = n_e^\downarrow = n_e/2$.

Typical parameters considered in this work are $r_s = 2$ (electron number density of $n = 2.01 \times 10^{29}$ m^{-3}) and $\Theta = 1$ ($T = 12.53$ eV $= 145.4$ kK).

B. X-ray Thomson scattering experiments

In spectrally resolved XRTS experiments[17] (Fig. 1), a detector instrument (usually a crystal spectrometer coupled to a CCD or microchannel plate) placed at some orientation relative to an incident monochromatic source of probing x-ray photons measures in each pixel an energy $E_{pixel} \in [E_s, E_s + \Delta E]$ over the source duration:

$$E_{pixel} = \int_0^{t_{probe}} dt \int_{E_s/\hbar}^{(E_s + \Delta E)/\hbar} d\omega_s \frac{\partial P_s}{\partial \omega_s}$$

$$\approx \frac{\Delta E}{\hbar} \int dt \frac{\partial P_s}{\partial \omega_s}\bigg|_{\hbar\omega_s = E_s + \Delta E/2}. \quad (2)$$

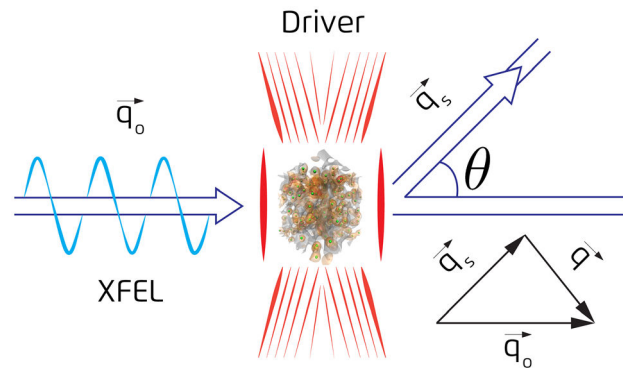**FIG. 1.** Sketch of a typical WDM experimental setup. The sample is compressed using a powerful long-pulse laser ("Driver" from top and bottom). The diagnostics is provided by a highly brilliant x-ray beam ("XFEL" from the left) with a variable delay time relative to the drive laser. A number of detectors is placed at different scattering angles θ behind the target to record the scattering signal.

In Eq. (2), $E_s = \hbar\omega_s$ is the energy of the scattered x rays, ΔE is the energy range associated with the pixel as determined by the properties (crystal orientation and dispersion relation, etc.) of the experimental apparatus, and $\partial P_s/\partial\omega_s$ is the scattered power per unit frequency as seen by the detector. The meaning of the approximation in Eq. (2) is that the differential scattered power is treated as constant over each pixel and, thus, is evaluated at the mid-point frequency of the energy interval.

1. Differential scattered power spectrum

As discussed by Fortmann *et al.*,[36] the differential scattered power spectrum can be written in terms of a more general, higher-order differential quantity,

$$\frac{\partial P_s}{\partial\omega_s} = \int d\mathcal{V} \int d\Omega \; \frac{\partial^3 P_s}{\partial\mathcal{V}\partial\Omega\partial\omega_s}$$
$$= \int d\mathcal{V} \int d\Omega \left(I_0 \, n_e \frac{\partial^2\tilde{\sigma}}{\partial\Omega\partial\omega_s} \right). \qquad (3)$$

In the above, I_0 is the intensity of the incident x rays, n_e is the mean electron number density in the volume element $d\mathcal{V}$, and $\partial^2\tilde{\sigma}/\partial\Omega\partial\omega_s$ is the double-differential generalized scattering cross section per unit solid angle, per unit frequency (see the discussion in Appendix A). For an interacting many-electron system, in which relativistic effects can be neglected, the latter can be written[37]

$$\frac{\partial^2\tilde{\sigma}}{\partial\Omega\partial\omega_s} = \frac{\omega_s}{\omega_0}\frac{\partial\tilde{\sigma}}{\partial\Omega}\bigg|_T S(\mathbf{q},\omega) \qquad (4)$$

in terms of the differential Thomson cross section with respect to the solid angle $\partial\tilde{\sigma}/\partial\Omega|_T$ and the total electron–electron dynamic structure factor (DSF), $S(\mathbf{q},\omega)$.

The DSF encodes all the information on spatiotemporal correlations between the electrons and is sensitive to the thermodynamic state of the system via different processes depending on the degree of collectivity exhibited by the electrons.[38] The latter is typically assessed by comparing the length scale probed by the radiation (roughly $1/q$) and a screening length λ_{scr}, i.e.,

$$\alpha = \frac{1}{q\lambda_{scr}}, \qquad (5)$$

commonly referred to as the "scattering parameter."[39] For states with $\alpha \ll 1$, the shape of the bulk of the scattered spectrum, i.e., the component traditionally thought of as being due to "free" electrons and is most readily accessible to XRTS experiments, is determined by the distribution function along the direction of $\mathbf{q}$. Thus, it is principally sensitive to the electron temperature when $\Theta \gg 1$ but gradually becomes an indicator of the electron number density as well when quantum degeneracy begins to manifest, i.e., for $\Theta \lesssim 1$. The collective regime, characterized by $\alpha \gg 1$, instead shows distinct resonances in the spectrum as the energy transfer from the probe is in phase with collective electronic density excitations, e.g., the plasmon mode. Here, the sensitivity of the spectrum to the thermodynamic state becomes much more complicated due to the competing roles of collisionless (Landau) and collisional damping, and the resulting dispersion relations. As will be discussed in this paper, one of the main strengths of the ITCFT technique is that it works equally well, and with similar accuracy,

across a range of scattering parameters. We consider conditions and wave number shifts that sample a wide range of values: 0.2 (single-particle) $< \alpha <$ 3.4 (collective).

2. Realistic restrictions for data analysis

If the x-ray source has close-to-uniform spatial and temporal intensity profiles, the volume of plasma probed by the x rays is sufficiently small (relative to its distance from both the source and detector) and is also reasonably homogeneous, and then the volume integration in Eq. (3) can be ignored, and the solid angle integration can be approximated by multiplying by the subtended solid angle element $d\Omega$. There are numerous approximate treatments of incorporating spatial inhomogeneity within the target,[40–43] and the incorporation of such effects into the present analysis framework remains an important task for future works. The same is true for the effect of *k*-blurring, which may be important for large sample volumes in close proximity to a divergent x-ray source. Fortunately, both of these considerations are usually negligible for XFEL experiments. A dedicated discussion related to these restrictions is required and, thus, shall not be addressed further here.

Assuming the foregoing conditions are, indeed, fulfilled, then the power spectrum reduces to (see Appendix A)

$$\frac{\partial P_s}{\partial\omega_s} \approx I_0 \, r_e^2 \, G(\theta,\phi) \, d\Omega \, n_e \mathcal{V}_s \left(\frac{\omega_s}{\omega_0}\right)^2 S(\mathbf{q},\omega), \qquad (6)$$

where $\mathcal{V}_s$ is the volume of the plasma interrogated by the probe, as seen from the position of the detector. The geometric term can be written in the following simplified forms for the bulk of cases of interest:[39]

$$G(\theta,\phi) = \begin{cases} 1 - \sin^2\theta\cos^2\phi & : \text{(linearly polarized)}, \\ \dfrac{1}{2}(1+\cos^2\theta) & : \text{(unpolarized)}. \end{cases} \qquad (7)$$

The shifts in the incident frequency and wave vector are given straightforwardly by energy and momentum conservation, i.e., $\omega = \omega_0 - \omega_s$ and $\mathbf{q} = \mathbf{q}_0 - \mathbf{q}_s$ (see the inset of vector triangle in Fig. 1). For any isotropic distribution function, it is well known that the DSF depends only on the magnitude of the wave vector shift, $q = |\mathbf{q}|$, which can be obtained by straightforward application of the cosine formula,

$$q = q_{full} = \left(q_0^2 + q_s^2 - 2q_0 q_s \cos\theta \right)^{1/2}. \qquad (8)$$

Ignoring dispersion of the probing radiation in the target (a condition universally satisfied for multi-keV x rays), one may reduce Eq. (8) to the commonly used approximate form (see Appendix B)

$$q \approx q_{approx} = 2q_0 \sin(\theta/2) \qquad (9)$$

and correspondingly ignore the factor $(\omega_s/\omega_0)^2 \approx 1$ in Eq. (6), thereby reducing the scattered power spectrum to a single dynamic term (the DSF). The robustness of this approximation plays an important role in the basis of the novel diagnostic method discussed in this paper.

To emphasize this point, Fig. 2 shows the percentage difference between the full (8) and approximate (9) forms of the wave number q as a function of scattered energy E_s and scattering angle θ for the example of the collective scattering data taken by Glenzer *et al.*[26]
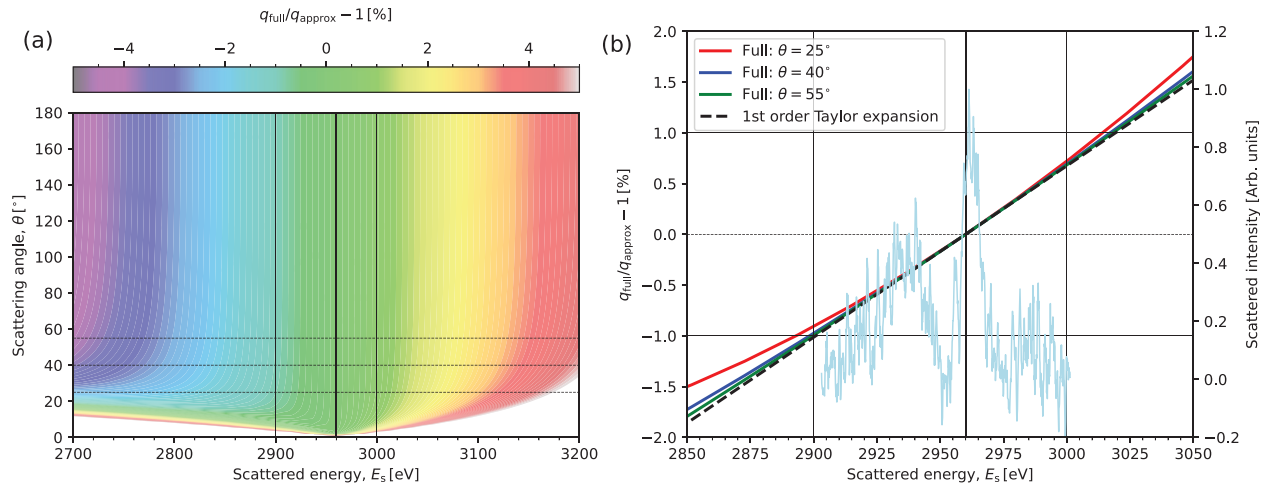
FIG. 2. (a) Contour map of the percentage difference of the full and approximate forms of the wave number shift as a function of scattered energy and scattering angle. This example shows the plasmon scattering data of Glenzer et al.[26] using x rays produced by Cl Ly-α line emission at $E_0 = 2.96$ keV. The thin vertical black lines denote the approximate dynamic range of the data. The three dashed horizontal lines at scattering angles of 25°, 40°, and 55° correspond to the minimum, mean, and maximum angles observed by the detector (the mean angle of 40° dominates the scattering intensity). (b) Slices through the contour map at the three scattering angles of interest (red, blue, and green solid curves). The first-order (linear in scattered energy) contribution to the Taylor expansion of the full wave number shift is shown by the black dashed curve. In this panel, the background-subtracted experimental data of Glenzer et al. are plotted on the right-hand axis (noisy, pale blue curve). It is clear that within the dynamic range of the data, the approximate form of the wave number shift is accurate to within 1%.

Clearly, the approximate expression (9) is well-fulfilled over the entire dynamic range of the experiment ($< \pm 1\%$ within the central region bounded by the vertical thin black lines). Similar results are found for all other cases considered. Despite the nonlinearity of the physics governing the response of the plasma to the probing radiation (e.g., the Landau damping rate of plasmons[38]) with respect to q, the small differences between the full and approximate forms of q will have a negligible impact on the shape of the scattered power spectrum. Nevertheless, a correction factor based on a first-order Taylor expansion of the full form of the wave number shift, $q_{1st\ order} = q_{approx}(1 - \omega/2\omega_i)$, could be incorporated for more accurate results; this will be considered in future work. In contrast to the results for XRTS, however, it should be noted that this approximation often does not hold for low-energy probes (particularly for the visible-wavelength lasers used in optical Thomson scattering to probe samples with the plasmon frequency being only slightly lower than the laser frequency, e.g., see Refs. 44–46), meaning that our diagnostic is currently limited to analyzing XRTS experiments; examination of possible extensions of ITCFT to cases with low-energy probes will be considered in detail in future works.

3. X-ray source profile and detector response

Finally, the spectral bandwidth and features of the x-ray source, be it either a relatively narrow, single sharp peak, such as those produced by XFELs,[47–49] or the more structured emission typical of thermal line emission from hot plasmas,[50,51] can be accommodated by convolving the scattered power spectrum with both the source function $\Sigma(\omega)$ and the response function of the detector $\Delta(\omega)$. In practice, only information of the convolution $R(\omega) = \Sigma(\omega) \circledast \Delta(\omega)$ [see also Eq. (10)] can be known, e.g., by performing a source characterization experiment. With the foregoing considerations and in the absence of an absolutely calibrated detector, one may dispense with all the

contributions to $\partial P_s/\partial \omega_s$ other than the remaining dynamic terms, working instead with a reduced intensity,

$$I(\mathbf{q}, \omega) = S(\mathbf{q}, \omega) \circledast R(\omega)$$
$$= \int_{-\infty}^{\infty} d\omega'\, S(\mathbf{q}, \omega') R(\omega' - \omega). \tag{10}$$

Consequently, in a realistic XRTS experiment, wherein the probe has some finite bandwidth and/or spectral structure, the energy received by the detector on each pixel can be approximately reduced from Eq. (2) to

$$E_{pixel} \approx A \frac{\Delta E}{\hbar} \int_0^{t_{pulse}} dt\, I(\mathbf{q}, \omega)|_{\hbar\omega_s' = E_s + \Delta E/2}, \tag{11}$$

where the factor A represents all the remaining factors that contribute to the magnitude of the energy in the pixel not included in the reduced intensity $I(q, \omega)$. Finally, if the state of the plasma under study evolves slowly compared to the duration of the x-ray probe, then the integration over time reduces to multiplying by t_{probe} and one finds

$$E_{pixel} \propto I(\mathbf{q}, \omega_0 - \omega_s'), \tag{12}$$

where ω_s' is the frequency associated with the characteristic energy discriminated by the pixel. From Eq. (12), and since it is extremely rare for the detectors used in XRTS experiments to be absolutely calibrated, it suffices to describe the measured intensity spectrum solely in terms of the reduced intensity Eq. (10).

C. Dynamic structure factor

A very general and convenient definition of the DSF is obtained from the Fourier transform of the microscopic density–density autocorrelation function,

$$S(\mathbf{q}, \omega) = \mathcal{F}[F(\mathbf{q}, t)]$$
$$= \int_{-\infty}^{\infty} dt \, e^{i\omega t} F(\mathbf{q}, t). \qquad (13)$$

The latter is also known as the intermediate scattering function (ISF) in the literature[17] and is given by

$$F(\mathbf{q}, t) = \langle \hat{n}(\mathbf{q}, t)\hat{n}(-\mathbf{q}, 0)\rangle \qquad (14)$$

with $\hat{n}(\mathbf{q}, t)$ being the density operator (expressed here in reciprocal space) at time t. We note that $\langle \cdots \rangle$ denotes a thermodynamic expectation value.

In thermodynamic equilibrium, the Hamiltonian $\hat{H}$ does not explicitly depend on t, and the DSF obeys a detailed balance relation between positive and negative frequency shifts,[52]

$$S(\mathbf{q}, -\omega) = e^{-\beta\hbar\omega} S(\mathbf{q}, \omega). \qquad (15)$$

Equation (15) implies that a scattered photon can either lose $[S(\mathbf{q}, \omega)]$ or gain $[S(\mathbf{q}, -\omega)]$ the amount of energy $\Delta E(\omega) = \hbar\omega$, and the ratio of the respective probabilities is given by the statistical factor of $e^{-\beta\hbar\omega}$. In the ground state, an energy gain is not possible leading to $S(\mathbf{q}, \omega < 0) \to 0$ as $\beta \to \infty$. In principle, Eq. (15) would directly allow one to extract the temperature from a given $S(\mathbf{q}, \omega)$ if it includes both positive and negative frequencies. In particular, it has the considerable advantage that no theoretical model for $S(\mathbf{q}, \omega)$ is required, and the corresponding analysis would be exact. Yet, the convolved XRTS intensity [Eq. (10)] does not fulfill Eq. (15). Moreover, the deconvolution of the intensity to obtain the actual DSF is, in general, rendered highly unstable by the noise in the experimental signal and is, therefore, not readily realizable in most cases. Although an approximate utilization of the detailed balance relation might still be possible in some cases,[53] its key advantages, being (a) exact and model-free and (b) generally applicable, cannot be leveraged.

As a consequence of the foregoing restrictions, the de facto procedure for inferring the temperature (as well as a host of other system parameters, such as the electron number density n_e or ionization degree $\langle Z \rangle$) from experimental XRTS data has become:[17-19] (1) construct a suitable model $S_{\mathrm{model}}[T](\mathbf{q}, \omega)$ for the DSF, (2) perform the convolution with the function $R(\omega)$, and (3) compare it to the experimentally measured intensity $I(\mathbf{q}, \omega)$, typically, within a nonlinear regression framework, such as Bayesian optimization.[54] In this way, the originally unknown parameters such as the temperature T are effectively reconstructed from a fit to the XRTS signal. Naturally, this approach strongly relies on the utilized model description for $S(\mathbf{q}, \omega)$, which can substantially affect the obtained free parameters. For example, Gregori et al.[19] have suggested using the Chihara decomposition,[24] where the total DSF is split into separate contributions from bound electrons, free electrons, and transitions between the two. Yet, the validity of this chemical picture is particularly questionable in the WDM regime, where electrons can be weakly localized around the ions.[55]

The present state-of-the-art appeals to the Kubo–Greenwood (KG) formalism, based on eigenvalues and occupations of the Kohn–Sham density functional theory[56-58] for obtaining the dielectric function in the optical limit. It can subsequently be extended to all wave numbers in terms of the Mermin dielectric function, with the required collision frequencies calculated from the KG dielectric function.[59]

A more sophisticated alternative is the use of time-dependent density functional theory (TD-DFT) simulations,[55,60,61] an in-principle exact method for determining the quantum dynamics of electrons under external time-dependent perturbations. TD-DFT presupposes neither an artificial decomposition nor a continuation from the optical limit. On the other hand, present implementations of TD-DFT rely on approximations that might limit their utility under WDM conditions. The development of more accurate exchange-correlation approximations beyond the adiabatic approximation is an active area of research.[62-72] Moreover, the considerable computational cost of TD-DFT calculations makes them impracticable as a method for optimizing over a wide range of parameters required for reproducing XRTS signals. Currently, this rules out TD-DFT for on-the-fly interpretation of experiments.

Finally, we note that, despite impressive recent progress, the reliable modeling of $S(\mathbf{q}, \omega)$ using potentially more accurate methods such as non-equilibrium Green functions[73,74] or even exact path integral Monte Carlo methods[75-77] is presently not feasible for realistic WDM applications. Moreover, the inevitable systematic errors of less accurate methods such as the Chihara decomposition are expected to become more pronounced for complex materials, such as the ablator coating of an ICF fuel capsule[9] or complex mixtures of elements that occur in planetary interiors.[78]

D. Temperature extraction in the Laplace domain

Let us next consider the two-sided Laplace transform of the dynamic structure factor,

$$\mathcal{L}[S(\mathbf{q}, \omega)] = \int_{-\infty}^{\infty} d\omega \, e^{-\tau\omega} S(\mathbf{q}, \omega)$$
$$= F(\mathbf{q}, \tau). \qquad (16)$$

In fact, Eq. (16) directly corresponds to the intermediate scattering function [Eq. (14)] but evaluated at an imaginary-time $\tau = it$, the values of which are in the range $\tau \in [0, \hbar\beta]$ due to the periodicity of the electron Green's functions at non-zero temperatures on this interval.[79] Thus, we write

$$F(\mathbf{q}, \tau) = \langle \hat{n}(\mathbf{q}, \tau)\hat{n}(-\mathbf{q}, 0)\rangle. \qquad (17)$$

Such imaginary-time correlation functions[28,33] emerge naturally within Feynman's path integral picture of statistical mechanics[30] and give access to a wealth of linear[75,80,81] and nonlinear[33] response properties of a given system. In particular, Eq. (16) often constitutes the starting point for an analytic continuation,[82] where one tries to reconstruct $S(\mathbf{q}, \omega)$ based on highly accurate path integral Monte Carlo data for the imaginary-time ISF $F(\mathbf{q}, \tau)$.

In the context of the present work, the main utility of $F(\mathbf{q}, \tau)$ is its symmetry in the imaginary-time domain about the special value,

$$\tau_{1/2} \equiv \hbar\beta/2. \qquad (18)$$

This fundamental property follows on directly from inserting the detailed balance relation [Eq. (15)] into Eq. (16) and using the symmetry of the integrands to reduce the integration interval to positive frequencies only, i.e.,

$$F(\mathbf{q}, \tau) = \int_0^\infty d\omega \, S(\mathbf{q}, \omega)\left\{e^{-\tau\omega} + e^{-\omega(\hbar\beta-\tau)}\right\}$$
$$= F(\mathbf{q}, \hbar\beta - \tau). \qquad (19)$$

In practice, $F(\mathbf{q}, \tau)$ has a unique minimum at $\tau_{1/2}$ [cf. Fig. 3(b)], and, thus, the location of this minimum directly determines the temperature of the system.

The final obstacle on the way toward the exact, model-free extraction of the temperature from an XRTS measurement is then the convolution with the instrument function $R(\omega)$, Eq. (10). It is easy to see that the two-sided Laplace transform of the intensity, $\mathcal{L}[S(\mathbf{q}, \omega) \circledast R(\omega)]$, does not obey the symmetry of Eq. (19). Conveniently, this problem can be fully overcome by making use of the well-known convolution theorem,

$$\mathcal{L}[S(\mathbf{q}, \omega)] = \frac{\mathcal{L}[S(\mathbf{q}, \omega) \circledast R(\omega)]}{\mathcal{L}[R(\omega)]} . \qquad (20)$$

Naively, the direct evaluation of the LHS of Eq. (20) gives straightforward access to the temperature of any given system. Upon closer inspection, however, it does require the explicit deconvolution of Eq. (10), which is rendered numerically highly unstable by the noise in the experimental signal. The evaluation of the enumerator of the RHS, on the other hand, is very robust with respect to noise due to its definition as an integral over the entire relevant frequency range. Moreover, the impact of the instrument function is completely removed by the denominator $\mathcal{L}[R(\omega)]$, which, too, can be evaluated without issue, provided its spectral profile decays sufficiently quickly for the Laplace transform to converge. In other words, Eq. (20) directly implies that it is possible to extract the exact temperature of a given system from an XRTS measurement without the need for an explicit deconvolution and, at the same time, without the bias due the broadening by the instrument function.

E. Integration range and convergence

It is easy to see that the symmetry relation Eq. (19) holds for any symmetric integration range, i.e., $F_{ab}(\mathbf{q}, \tau) = F_{ab}(\mathbf{q}, \hbar\beta - \tau)$ with

$$F_{ab}(\mathbf{q}, \tau) = \int_{-b}^{-a} d\omega \, S(\mathbf{q}, \omega) e^{-\tau\omega} + \int_{a}^{b} d\omega \, S(\mathbf{q}, \omega) e^{-\tau\omega}$$

$$= \int_{a}^{b} d\omega \, S(\mathbf{q}, \omega) \left\{ e^{-\tau\omega} + e^{-\omega(\hbar\beta - \tau)} \right\}. \qquad (21)$$

Therefore, deconvolved data for $S(\mathbf{q}, \omega)$ would only be required on a finite frequency interval for both positive and negative values of ω. On the other hand, the proof of the convolution theorem of the two-sided Laplace transform explicitly requires the infinite integration range. Yet, in an XRTS experiment, the intensity is measured in a finite frequency range $\omega \in [\omega_{\min}, \omega_{\max}]$ with reasonable accuracy.

Hence, we define the symmetrically truncated Laplace transform of the XRTS signal as

$$\mathcal{L}_x[S(\mathbf{q}, \omega) \circledast R(\omega)] = \int_{-x}^{x} d\omega \, e^{-\tau\omega} \left\{ S(\mathbf{q}, \omega) \circledast R(\omega) \right\} \qquad (22)$$

with the corresponding truncated imaginary-time ISF

$$F_x(\mathbf{q}, \tau) = \frac{\mathcal{L}_x[S(\mathbf{q}, \omega) \circledast R(\omega)]}{\mathcal{L}[R(\omega)]} . \qquad (23)$$

Clearly, it holds

$$\lim_{x \to \infty} F_x(\mathbf{q}, \tau) = F(\mathbf{q}, \tau), \qquad (24)$$

and the convergence with respect to x can simply be checked in practice.

III. RESULTS: SYNTHETIC DATA

In this section, we illustrate the utility of our new ITCFT methodology by performing synthetic data analysis. For this purpose, we generate synthetic scattering spectra based on the DSF of a uniform electron gas model[75,76,83] (see Appendix D for details) and a simple model for the Rayleigh feature using a Gaussian function centered at $\omega = 0$. For the electronic contribution, we take the DSF arising from a
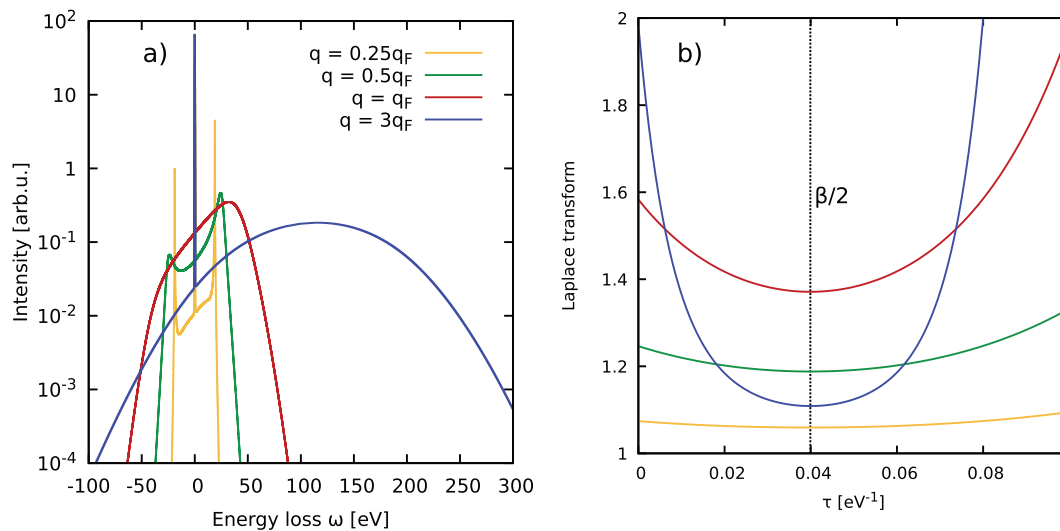

FIG. 3. (a) Synthetic data of the (unconvolved) dynamic structure factor $S(\mathbf{q}, \omega)$ at $r_s = 2$ and $\Theta = 1$ ($T = 12.53$ eV) for different values of the wave number $q = |\mathbf{q}|$. (b) Corresponding imaginary-time intermediate scattering functions $F(\mathbf{q}, \tau) = \mathcal{L}[S(\mathbf{q}, \omega)]$. We note the perfect symmetry around $\tau_{1/2}$ (vertical dotted black line) for all q.

neural-network representation of the static local field correction of the uniform electron gas.[80] The total DSF, therefore, has the following form:

$$S(\mathbf{q}, \omega) = S_{\text{UEG}}(\mathbf{q}, \omega) + \frac{e^{-\omega^2/2\eta^2}}{\sqrt{2\pi\eta^2}} . \tag{25}$$

In the above, η is the standard deviation of the Gaussian component. In particular, the last term on the RHS becomes a delta distribution in the limit of $\eta \to 0$. In practice, we use $\eta = \omega_{\text{pe}}/100$ for numerical convenience.

Note that throughout this section, we plot all (synthetic and experimental) data for the intensity as a function of the energy loss $\hbar\omega = \hbar\omega_0 - \hbar\omega_s$ and not directly as a function of the scattered energy $\hbar\omega_s$. Therefore, the plots appear reflected compared to the original reference material.[18,26] However, we feel that this choice gives the reader a more intuitive connection to the two-sided Laplace transform Eq. (16), in general, and the role of the exponential factor $e^{-\tau\omega}$, in particular, which are of central importance for the current work.

A. Imaginary-time intermediate scattering function

To begin with, we compute the imaginary-time correlation function from our simple DSF model (see Fig. 3) for relevant values of the wave number q at the electronic Fermi temperature $\Theta = 1$ ($T = 12.53$ eV) and a metallic density of $r_s = 2$. By design, all DSFs exhibit the same sharp elastic feature around $\omega = 0$. The yellow curve corresponding to a quarter of the Fermi wave number $q = 0.25 q_F$ exhibits a sharp plasmon peak around $\omega = 25$ eV. Upon increasing q, the plasmon is first broadened (green curve, $q = 0.5 q_F$) and then disappears in a single broad inelastic curve at $q = q_F$ (red). Finally, the blue curve computed for a large wave number $q = 3 q_F$ in the non-collective, single-particle regime exhibits a broad Gaussian form, and its peak position increases parabolically with q. Figure 3(b) shows the corresponding imaginary-time intermediate scattering function $F(\mathbf{q}, \tau) = \mathcal{L}[S(\mathbf{q}, \omega)]$, i.e., the two-sided Laplace transform of the DSF defined in Eq. (16). Evidently, the different curves substantially depend on the wave number, thereby reflecting the transition from the collective regime $q \ll q_F$ to the single-particle regime $q \gg q_F$. This has been analyzed in detail in the recent Ref. 29. At the same time, all curves are perfectly symmetric around the same value of $\tau_{1/2}$, as expected. Knowledge of the DSF, therefore, clearly allows for a straightforward extraction of the temperature for any value of the wave vector $\mathbf{q}$ without any physical assumptions or models, provided that the system is close to thermodynamic equilibrium.

We further illustrate the origin of this behavior by analyzing the frequency-resolved contribution to $F(\mathbf{q}, \tau)$ for $q = q_F$ in Fig. 4. More specifically, we plot $S(\mathbf{q}, \omega)e^{-\tau\omega}$ for three different values of the imaginary-time τ. The red curve corresponds to $\tau = 0$, i.e., to the original DSF that is also shown in Fig. 3(a). The green curve has been obtained for $\tau = \tau_{1/2} = \hbar\beta/2$, at which $F(\mathbf{q}, \tau)$ attains its minimum value. Evidently, the corresponding curve is symmetric around $\omega = 0$. This is a general property of the dynamic structure factor and can directly be seen by inserting the detailed balance relation Eq. (15) into the modified quantity $C(\mathbf{q}, \omega) = S(\mathbf{q}, \omega)e^{-\beta\hbar\omega/2}$,
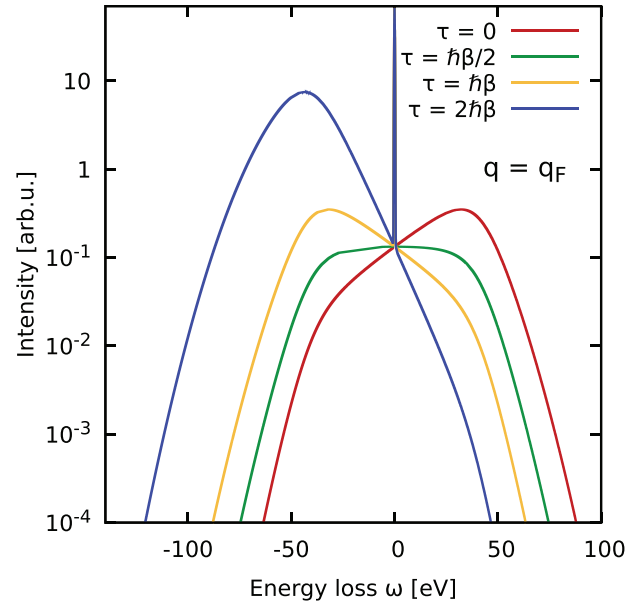

FIG. 4. Contribution to the two-sided Laplace transform $\mathcal{L}[S(\mathbf{q}, \omega)]$, $S(\mathbf{q}, \omega)e^{-\tau\omega}$, for synthetic data at $r_s = 2$, $\Theta = 1$ ($T = 12.53$ eV), and $q = q_F$ for selected values of the imaginary-time τ.

$$\begin{aligned}
C(\mathbf{q}, \omega) &= e^{-\beta\hbar\omega/2}S(\mathbf{q}, \omega) \\
&= S(\mathbf{q}, -\omega)e^{\beta\hbar\omega}e^{-\beta\hbar\omega/2} \\
&= S(\mathbf{q}, -\omega)e^{\beta\hbar\omega/2} \\
&= C(\mathbf{q}, -\omega).
\end{aligned} \tag{26}$$

The yellow curve has been obtained for $\tau = \hbar\beta$ and corresponds to the original DSF but mirrored around $x = 0$. For completeness, we also include a curve for $\tau = 2\hbar\beta$, which has no physical equivalent in Feynman's imaginary-time path integral picture, but can be easily computed from the two-sided Laplace transform Eq. (16). In this case, the negative frequency range gets substantially enhanced by the exponential factor, whereas, conversely, the positive frequency range gets damped. In practice, the evaluation of Eq. (16) at such large values of τ would require high-quality data of the DSF at very low frequencies, which is unrealistic at present. At the same time, we note that it is not needed to locate the minimum and hence extract the temperature.

To conclude the analysis of the unconvolved DSF, we directly consider the impact of the temperature on the DSF and its Laplace transform. This is shown in Fig. 5 in the collective regime ($q = 0.5q_F$, left column) and in the single-particle regime ($q = 3q_F$, right column). In particular, Fig. 5(a) shows the DSF evaluated from the usual UEG model at different values of the temperature; beware that the elastic peak of the depicted synthetic model data does not depend on Θ. The yellow curve has been obtained for $\Theta = 0.25$ ($T = 3.13$ eV) and exhibits sharp plasmon peaks around $\omega = \pm 20$ eV. Increasing the temperature by a factor of two ($\Theta = 0.5$, $T = 6.26$ eV) yields the black curve where the impact of increasing thermal effects is twofold: first, the DSF is broadened overall and decays more slowly for large $|\omega|$; second, the plasmon is damped and shifted to significantly larger frequencies both in the positive and negative frequency domains.
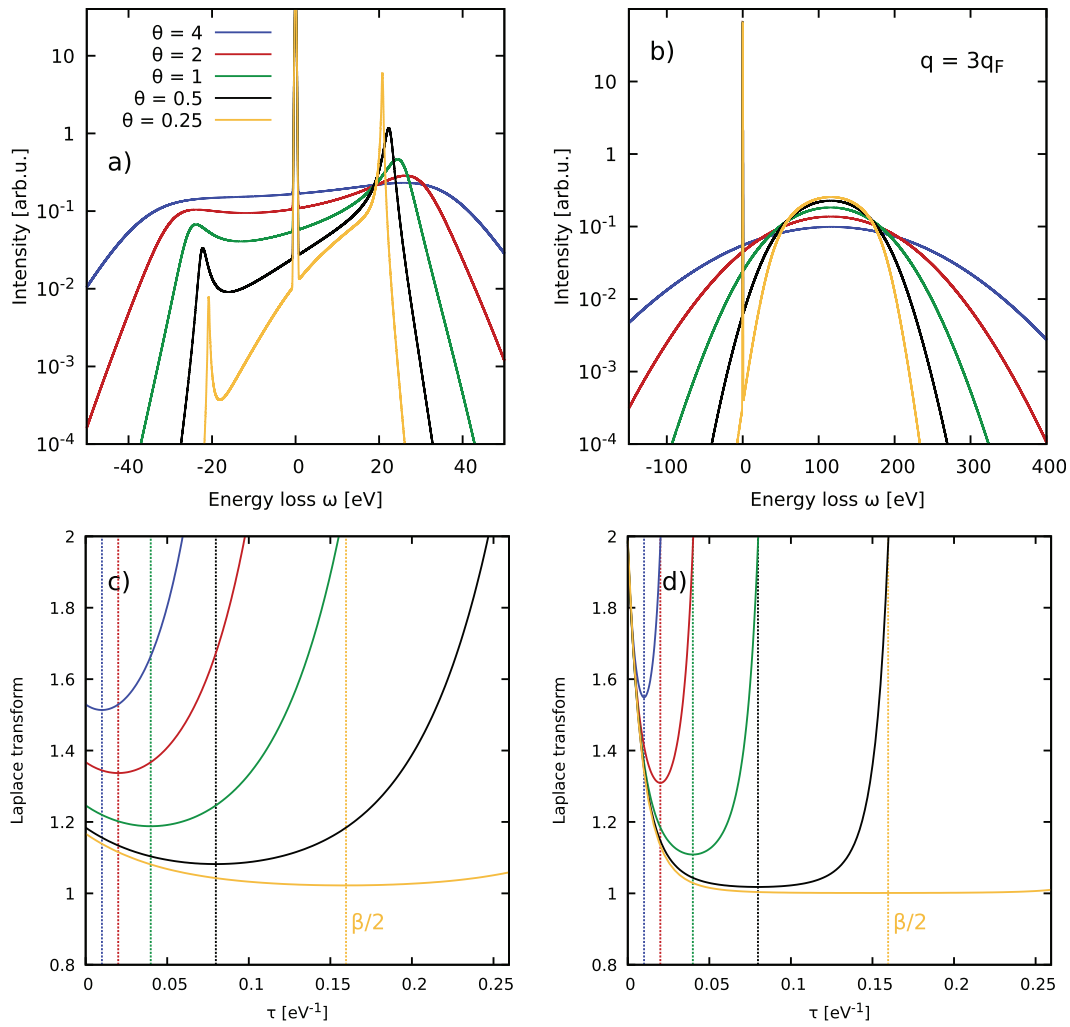
FIG. 5. Top row: Dynamic structure factor $S(\mathbf{q}, \omega)$ computed from a UEG model [Eq. (25)] for $r_s = 2$ and different values of the temperature parameter Θ (with $T_F = 12.53$ eV) at (a) $q = 0.5q_F$ (collective) and (b) $q = 3q_F$ (single-particle). Bottom row [(c) and (d)]: Corresponding imaginary-time intermediate scattering functions $F(\mathbf{q}, \tau) = \mathcal{L}[S(\mathbf{q}, \omega)]$. The respective minima at $\tau = \tau_{1/2} = \hbar\beta/2$ are indicated by the vertical dotted lines.

We note that approximate models for this plasmon shift[84] have been used to determine the temperature in previous XRTS experiments.[85] Increasing the temperature further to $\Theta = 1$ ($T = 12.53$ eV, green) enhances both the broadening and the plasmon shift, until the plasmon is eventually damped out for $\Theta = 2$ ($T = 25.06$ eV, red) and $\Theta = 4$ ($T = 50.12$ eV, blue).

The corresponding extraction of the temperature is illustrated in Fig. 5(c), where we show the respective data for the imaginary-time intermediate scattering function $F(\mathbf{q}, \tau) = \mathcal{L}[S(\mathbf{q}, \omega)]$; all curves are, of course, symmetric about $\tau_{1/2}$. For the lowest temperature, $F(\mathbf{q}, \tau)$ is very flat around the minimum, which might make the precise location of the latter more difficult in the case of noisy input data. Yet, this does not pose a fundamental obstacle and can easily be mitigated by considering the relation

$$F(\mathbf{q}, 0) = F(\mathbf{q}, \hbar\beta). \tag{27}$$

In other words, we can look where the two-sided Laplace transform of $S(\mathbf{q}, \omega)$ attains the same value as for $\tau = 0$ as an alternative way to determine β to circumvent potential problems associated with the occurrence of a shallow minimum in $F(\mathbf{q}, \tau)$.

Let us next consider the temperature dependence of the DSF in the non-collective regime, i.e., at $q = 3q_F$ depicted in Fig. 5(b). In this regime, all curves exhibit qualitatively similar broad peaks around $\omega = 120$ eV. The main impact of the temperature is given by the substantially more slowly vanishing tails for large ω for larger values of Θ and the less pronounced intensities of the DSF at negative frequencies at low Θ due to the detailed balance relation. In Fig. 5(d), we show the corresponding curves for $F(\mathbf{q}, \tau)$, which give the same correct values for the (inverse) temperature as in Fig. 5(c). Notably, the minimum in $F(\mathbf{q}, \tau)$ at $\Theta = 0.25$ is even more shallow than at $q = 0.5q_F$, which makes the usage of Eq. (27) even more essential.

B. Convolution with the instrument function

In Sec. III B, we have conclusively demonstrated that knowledge of the dynamic structure factor $S(\mathbf{q}, \omega)$ allows a straightforward extraction of the temperature independent of the wave number regime (collective vs single-particle) and without the need for any physical models or simulations. Yet, in a real scattering experiment, we do not have direct access to the DSF because the measured intensity $I(\mathbf{q}, \omega)$ is convolved with the instrument function $R(\omega)$ as stated in Eq. (10). We, therefore, analyze in detail the impact of the convolution on extracting the temperature across the relevant range of wave numbers q in Fig. 6.

The top row corresponds to the collective regime, where the inelastic part of the deconvolved DSF [solid yellow, Fig. 6(a)] exhibits a sharp plasmon peak around ± 20 eV. The dashed lines have been obtained by convolving the yellow curve with Gaussian model instrument functions of different widths σ. Evidently, the main effect of the convolution is a substantial broadening of the sharp features in the original DSF, which becomes more pronounced with increasing σ. Indeed, the convolved intensity appears to consist of a single broad elastic peak for $\sigma = \omega_p = 16.67$ eV, and no trace of the plasmon peaks can be recognized with the naked eye. In Fig. 6(b), we show the corresponding results for the two-sided Laplace transform of the intensity. As usual, the solid yellow line corresponds to the exact $F(\mathbf{q}, \tau) = \mathcal{L}[S(\mathbf{q}, \omega)]$, with a minimum about $\tau_{1/2}$ (vertical line). In addition, the dashed curves show results for the Laplace transform of the convolved curves $\mathcal{L}[I(\mathbf{q}, \omega)]$ for different σ. Evidently, the minimum in the Laplace transforms shifts to smaller τ with increasing width of the instrument function. In other words, the broadening from the convolution makes the extracted temperatures too large.[25] Given accurate knowledge of the instrument function $R(\omega)$, it might seem natural to attempt an explicit deconvolution of Eq. (10) to reconstruct the original DSF $S(\mathbf{q}, \omega)$. This, in turn, would allow one to subsequently obtain $F(\mathbf{q}, \tau) = \mathcal{L}[S(\mathbf{q}, \omega)]$ and, thus, to extract the temperature from the location of the unbiased minimum. In practice, such a deconvolution is notoriously unstable with respect to the noise in the input data, which usually prevents the explicit extraction of $S(\mathbf{q}, \omega)$. Yet, this obstacle is completely circumvented within the ITCFT methodology due to the convolution theorem in Eq. (20). Particularly, the instrument function and the DSF can be separated in a straightforward way in the Laplace domain. Consequently, we can completely remove the impact of the artificial broadening by dividing the dashed curves by the Laplace transform of the instrument function $\mathcal{L}[R(\omega)]$, which gives the original solid yellow curve in all cases.

For a Gaussian probe function of width σ and centered around $\omega = 0$, $R_\sigma(\omega)$, the two-sided Laplace transform can be carried out analytically,

$$\mathcal{L}[R_\sigma(\omega)] = e^{\sigma^2 \tau^2 / 2}. \qquad (28)$$

The results are shown as the dashed lines in Fig. 7 for the same values of σ as in Fig. 6. The vertical dotted yellow line indicates $\tau_{1/2}$ for $T = 12.53$ eV, i.e., $\Theta = 1$ at $r_s = 2$, and has been included as a reference. For the most narrow instrument function with $\sigma = 1.67$ eV, Eq. (28) attains a nearly constant value of one over the entire relevant τ-range. Consequently, the impact of the instrument function on $\mathcal{L}[I(\mathbf{q}, \omega)]$ is small, and the dashed blue line in Fig. 6(b) is very close

to the exact result for $F(\mathbf{q}, \tau) = \mathcal{L}[S(\mathbf{q}, \omega)]$. With increasing σ, $\mathcal{L}[R(\omega)]$ starts to increasingly deviate from unity, which manifests as a shift of the minimum in $\mathcal{L}[I(\mathbf{q}, \omega)]$ toward smaller values of τ.

In addition, we find that the particular value of x for which convergence is reached strongly increases with the width of the instrument function $R_\sigma(\omega)$. In other words, the integral boundaries for which the exact convolution theorem Eq. (20) is recovered scale with σ.

A further interesting point of this analysis is the required accuracy of the intensity needed to extract the exact value of $\tau_{1/2}$ and, thus, the temperature. For example, at $\sigma = 3.33$ eV, convergence is reached around $x = 25$ eV. In this case, the intensity [see Fig. 6(a)] at $\omega = -25$ eV is reduced by a single order of magnitude compared to the size of the plasmon peak at $\omega = 20$ eV. Resolving the inelastic intensity over such a range in a scattering experiment is feasible in modern laser facilities.[47–49] For the broadest instrument function with $\sigma = 16.67$ eV, the extracted temperature converges around $x = 75$ eV. Yet, here, the convolved intensity has already decayed by more than three orders of magnitude and, therefore, will be difficult to resolve in an actual experiment. This clearly illustrates the importance of a narrow probe function for the accurate and practical analysis of experimental scattering data.

To bring the discussion of Fig. 6(c) to a close, let us consider the dotted curves, which have been obtained by determining the minimum in $\mathcal{L}[I(\mathbf{q}, \omega)]$ without the correction by $\mathcal{L}[R(\omega)]$. We find that the finite width of the instrument function then substantially influences (in fact, decreases) the extracted values of $\tau_{1/2}$ even in the case of the relatively narrow Gaussian with $\sigma = 1.67$ eV.

The bottom three rows of Fig. 6 contain the same analysis, but for increasing values of the wave number q. We, therefore, restrict ourselves here to a concise discussion of the main differences between the different regimes. First, we reiterate our earlier point about the increasing width of the unconvolved DSF with increasing q. This, in turn, means that the impact of the Gaussian instrument function becomes less pronounced for large q. Indeed, the uncorrected curves for both $\sigma = 1.67$ and $\sigma = 3.33$ eV are within 5% of the correct temperature in the single-particle regime [see Fig. 6(l)]. For the narrowest instrument function, this even holds at the Fermi wave number $q = q_F$ [see Fig. 6(i)]. As a second observation, we find that the convergence of the extracted temperature with the integration boundary x is shifted to somewhat larger frequencies. This is completely unproblematic for $\sigma \in [1.67, 3.33, 6.67]$ eV, as the width of the actual intensity increases similarly. Therefore, the intensity does not have to be resolved over substantially more than one order of magnitude. For $\sigma = 16.67$ eV, on the other hand, reaching convergence in practice will be difficult.

We further illustrate the impact of the instrument function on the two-sided Laplace transform of the intensity by showing both $I(\mathbf{q}, \omega)e^{-\tau\omega}$ (dashed) and $S(\mathbf{q}, \omega)e^{-\tau\omega}$ (solid) for $q = q_F$ in Fig. 8 for three relevant values of the imaginary-time τ. The green curves have been obtained for $\tau = 0$ and, thus, show the original intensity and DSF. The red curves correspond to $\tau_{1/2}$, where $F(\mathbf{q}, \tau)$ attains its minimum. In this case, the contribution to $\mathcal{L}[S(\mathbf{q}, \omega)]$ is symmetric around $\omega = 0$, whereas the convolution with $R(\omega)$ noticeably skews the corresponding curve to lower frequencies. This trend is even more pronounced for $\tau = \hbar\beta$ (blue curves), where $S(\mathbf{q}, \omega)e^{-\tau\omega}$ is equal to the
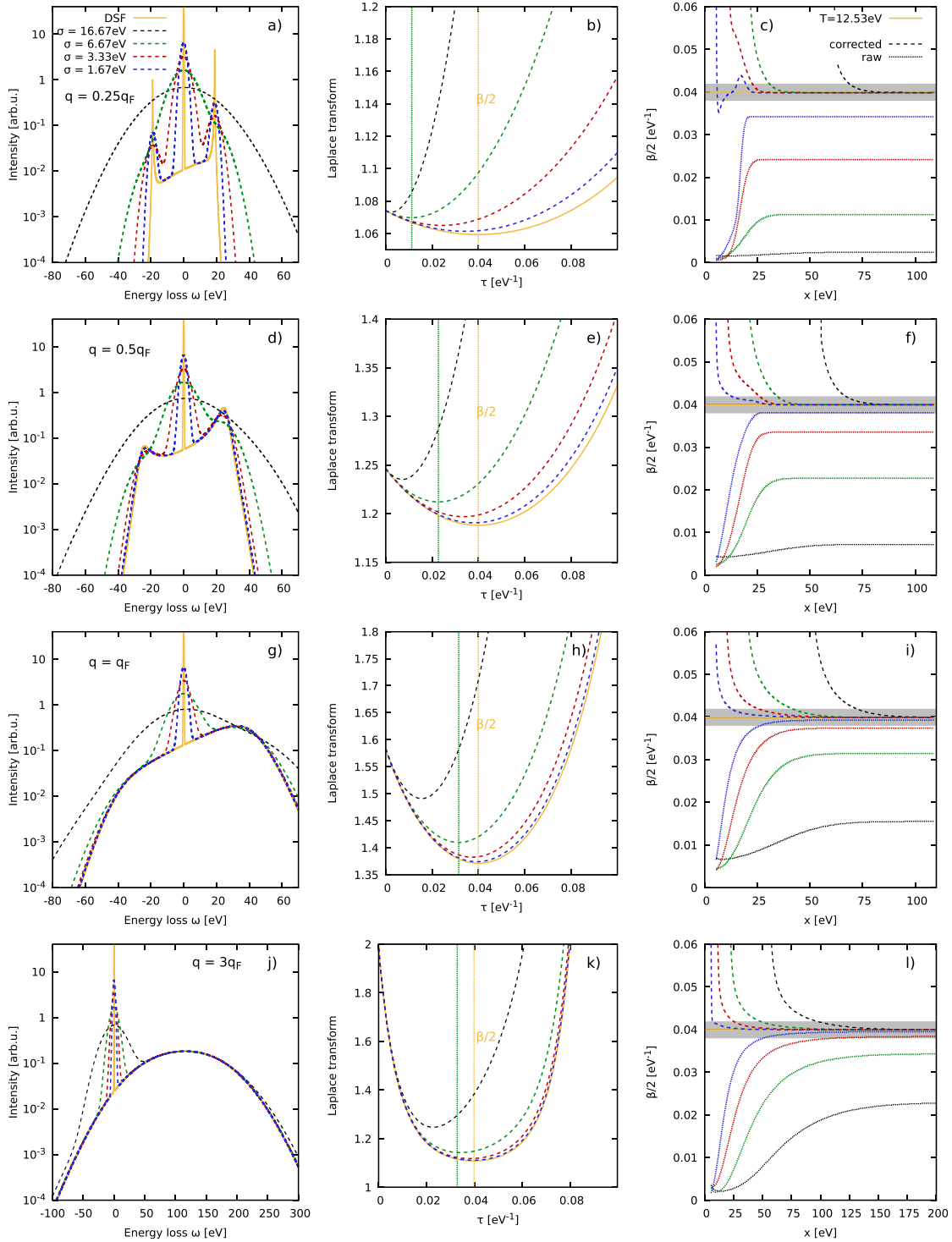
FIG. 6. Temperature extraction from synthetic UEG data for the convolved intensity $I(\mathbf{q}, \omega) = S(\mathbf{q}, \omega) \circledast R(\omega)$ [Eq. (10)] at $r_s = 2$ and $\Theta = 1$ ($T = 12.53$ eV). Left column [(a), (d), (g), (j)]: original DSF (solid yellow), and intensities obtain from convolutions with Gaussian $R(\omega)$ with different widths σ (dashed lines). Middle column [(b), (e), (h), (k)]: corresponding two-sided Laplace transforms of original (yellow) DSF and the convolved curves without the correction by $\mathcal{L}[R(\omega)]$. Right column [(c), (f), (i), (l)]: convergence of the temperature-extraction from the truncated Laplace transform $\mathcal{L}_x[I(\mathbf{q}, \omega)]$, Eq. (22), with respect to the integration boundary x. The dashed (dotted) curves have been obtained with (without) the correction due to $R(\omega)$, and the shaded gray areas indicate a 5% interval around the exact (yellow) temperature.
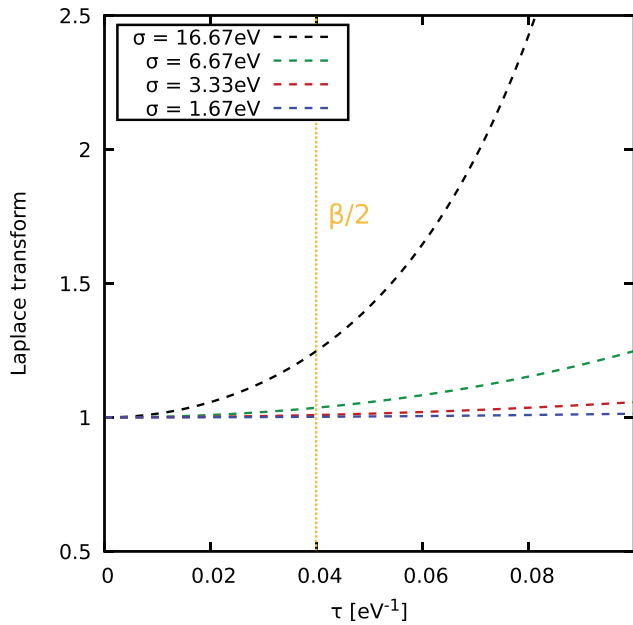
FIG. 7. Two-sided Laplace transform of the Gaussian instrument function $R_\sigma(\omega)$, see Eq. (28), for different relevant values of the width σ. The dotted yellow vertical line indicates $\tau_{1/2} = \hbar\beta/2$ for $T = 12.53$ eV, cf. Fig. 6, and has been included as a reference.

solid green curve mirrored around $\omega = 0$, whereas this clearly does not hold for the corresponding dashed curve.

We conclude this section with a more systematic analysis of the impact of the width of the instrument function σ on the extraction of the temperature, which is shown in Fig. 9. We plot the obtained values of $\beta = 1/k_B T$ as a function of σ for the four wave numbers considered in Fig. 6. The squares show the values where we have corrected for the impact of $\mathcal{L}[R(\omega)]$, and we find a perfect agreement with the exact temperature for all combinations of σ and q. The crosses show the extracted *raw* temperatures without this correction. Overall, all four curves exhibit the same qualitative trend: the error in the uncorrected temperature monotonically decreases with decreasing σ, as is expected. Moreover, the curves are strictly ordered with q, as large wave numbers correspond to broader DSFs, for which the impact of the convolution is less pronounced. The shaded gray area shows an interval of $\pm 5\%$ around the exact inverse temperature, which can be reached without the correction either for a very narrow instrument function or in the single-particle regime ($\alpha \ll 1$). This directly implies that large scattering angles as they can be realized in backscattering experiments make the method more robust against possible uncertainties in the characterization of the instrument function $R(\omega)$.

C. Different temperatures

In Sec. III C, we analyzed in detail the impact of the wave number and the width of the instrument function on the extracted temperature from a convolved scattering intensity signal. In Fig. 10, we extend these considerations by analyzing different values of the temperature Θ.

FIG. 9. Temperature extraction at $r_s = 2$ and $\Theta = 1$ ($T = 12.53$ eV) as a function of the width σ of the Gaussian instrument function for different wave numbers q. Squares (crosses): corrected (uncorrected) for influence of $\mathcal{L}[R(\omega)]$. Horizontal yellow: exact inverse temperature. Shaded gray area: interval of $\pm 5\%$, included as a reference.
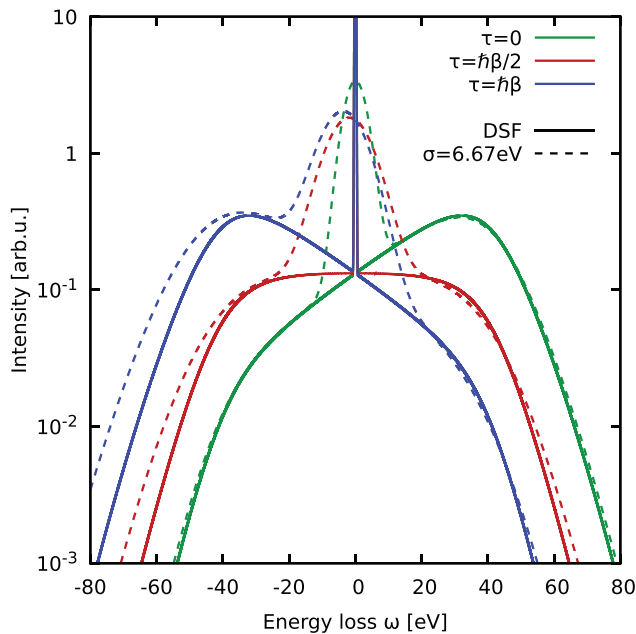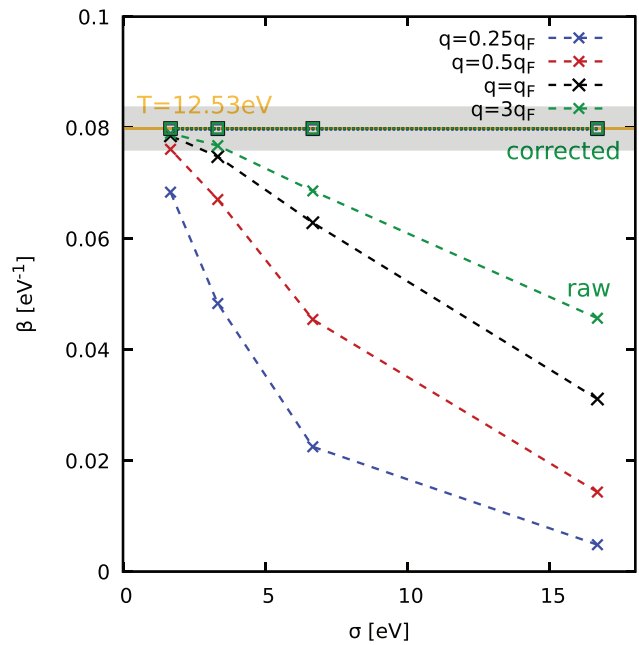

FIG. 8. Contribution to the two-sided Laplace transform $\mathcal{L}[S(\mathbf{q}, \omega)]$ (solid) and $\mathcal{L}[I(\mathbf{q}, \omega)]$ (dashed) as a function of the frequency ω at $r_s = 2$, $\Theta = 1$ ($T = 12.53$ eV), and $q = q_F$ for selected values of the imaginary-time τ.
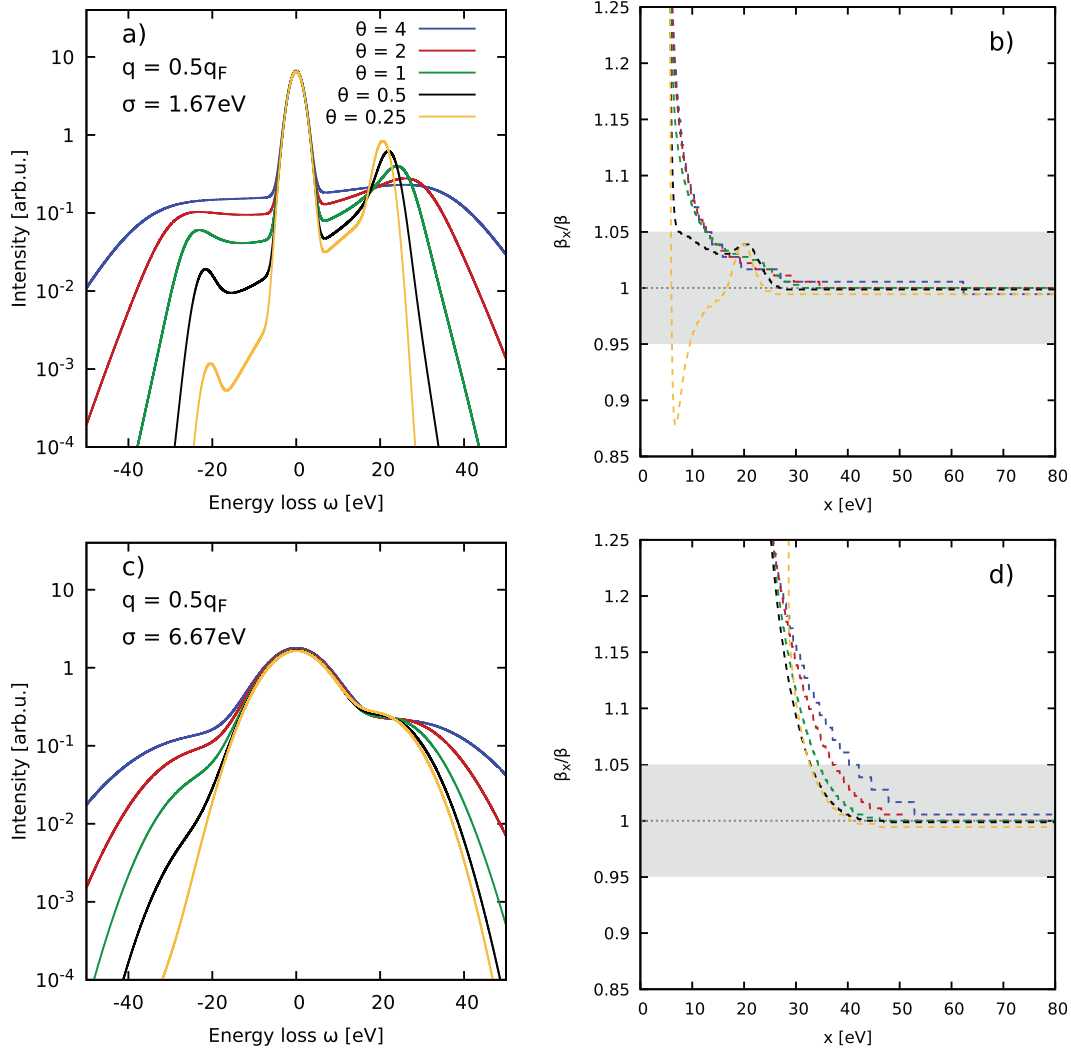
FIG. 10. Influence of the temperature parameter Θ (with $T_F = 12.53$ eV) on the extraction of the temperature at $r_s = 2$ and $q = 0.5q_F$. Top (bottom) row: width of the instrument function $\sigma = 1.67$ eV ($\sigma = 6.67$ eV). Left [(a) and (c)]: convolved scattering intensity. Right [(b) and (d)]: convergence of the extracted inverse temperature with the integration boundary x, rescaled by the corresponding exact value of β. The shaded gray area indicates an interval of $\pm 5\%$ and has been included as a reference.

Figure 10(a) shows results for $I(\mathbf{q}, \omega)$ at $r_s = 2$ and $q = 0.5q_F$ for a narrow instrument function with $\sigma = 1.67$ eV. A comparison with the corresponding deconvolved results for the DSF (see Fig. 5) reveals the substantial broadening of the plasmon peak, in particular at low temperatures. The convergence of the extracted temperature with the integration boundary x is shown in Fig. 10(b). The curves have been rescaled by the respective value of β to allow for a more straightforward comparison. As usual, the shaded gray area indicates an interval of $\pm 5\%$ and has been included as a reference.

First, we find that the extracted temperature converges toward the exact value for all values of Θ, as is expected; the small deviations from one at large x are a mainly a consequence of the finite ω-resolution in the synthetic data for the intensity, and the finite τ-resolution in our numerical implementation. While the latter can be increased if necessary, the former is determined by the resolution of the employed detector in an experiment. In practice, the attained accuracy from the ITCFT method is limited not by this discretization error but by the experimental noise, cf. Sec. IV.

The values of x for which convergence is reached appear to be nearly independent of Θ. The accurate extraction of the temperature is thus substantially more challenging at low temperatures, where the scattering intensity at negative frequencies can be orders of magnitude smaller than in the positive ω range. For example, the negative plasmon is reduced by three orders of magnitude at $\Theta = 0.25$, whereas it is not even reduced by a full order of magnitude for $\Theta = 1$. From a practical perspective, this means that the accurate measurement of the intensity at $\omega < 0$ is of prime importance and decisively determines the quality of the extracted temperature for $\Theta \ll 1$, as $\omega > 0$ and $\omega < 0$ equally contribute to $F(\mathbf{q}, \tau_{1/2} = \hbar\beta/2)$, cf. Fig. 8.

The bottom row of Fig. 10 shows the same analysis for a broader instrument function with $\sigma = 6.67$ eV. Overall, the conclusions are similar to the previous case, although we do find a more pronounced dependence of the convergence with x on Θ. Still, the importance of the negative frequency range remains the same.

An interesting insight on which we close the current discussion can be made by analyzing the effect of the temperature parameter on the convolved intensity in the single-particle regime. The corresponding results are shown in Fig. 11 for a narrow probe function with $\sigma = 1.67$ eV. The main difference regarding the extraction of the temperature compared to the smaller wave number shown in Fig. 10 is that we had to use the relation Eq. (27) at $\Theta = 0.25$, as the minimum in $F(\mathbf{q}, \tau)$ is extremely shallow. Still, we resolve the correct temperature for all temperatures, and the effect of Θ on the value of x for which the convergence is reached is small. From this, one may conclude that the ITCFT technique does *not* merely amount to an alternative take on the use of detailed balance, as has already been extensively used elsewhere in the literature, since it remains viable across all regimes of the scattering (collectivity) parameter. In contrast, the method of temperature extraction via detailed balance as undertaken elsewhere is restricted in practice to the collective scattering regime where its manifestation on the relative amplitudes of the red- and blue-shifted plasmons can clearly be discerned in experimental data.

IV. ERROR ANALYSIS AND THE ROLE OF EXPERIMENTAL NOISE

In a real scattering experiment, the measured intensity $I_{\exp}(\mathbf{q}, \omega)$ is always afflicted with some form of random noise $\Delta I(\mathbf{q}, \omega)$, such that

$$I_{\exp}(\mathbf{q}, \omega) = I(\mathbf{q}, \omega) + \Delta I(\mathbf{q}, \omega), \quad (29)$$

with $I(\mathbf{q}, \omega)$ being the true convolution of $S(\mathbf{q}, \omega)$ and the instrument function $R(\omega)$. Throughout this analysis, we will assume perfect knowledge of the latter; the role of uncertainty in the instrument

function will be investigated in more detail in a separate publication. In the following, we will systematically investigate the impact of the noise on the symmetrically truncated Laplace transform of the experimental scattering signal, which is given by

$$\mathcal{L}_x[I_{\exp}(\mathbf{q}, \omega)] = \mathcal{L}_x[I(\mathbf{q}, \omega) + \Delta I(\mathbf{q}, \omega)]$$
$$= \mathcal{L}_x[I(\mathbf{q}, \omega)] + \mathcal{L}_x[\Delta I(\mathbf{q}, \omega)]. \quad (30)$$

In a counting-based scattering experiment, the error distribution is given by[86]

$$\Delta I(\mathbf{q}, \omega) = \xi_{\sigma_\Delta}(\omega)\sqrt{I(\mathbf{q}, \omega)}, \quad (31)$$

where $\xi_{\sigma_\Delta}(\omega)$ is a Gaussian random variable (centered around zero) with a variance σ_Δ. We note that Eq. (31) constitutes an idealized model and breaks down in practice when the effect of a background subtraction becomes noticeable, i.e., at large values of $|\omega|$.

Equations (30) and (31) imply that it is sufficient to analyze the symmetrically truncated Laplace transform of the product of Gaussian random noise of unit variance with the square root of the actual intensity, $\mathcal{L}_x[\xi_1(\omega)\sqrt{I(\mathbf{q}, \omega)}]$, as any particular noise level σ_Δ can simply be included as a pre-factor,

$$\mathcal{L}_x[I_{\exp}(\mathbf{q}, \omega)] = \mathcal{L}_x[I(\mathbf{q}, \omega)] + \sigma_\Delta \mathcal{L}_x[\xi_1(\omega)\sqrt{I(\mathbf{q}, \omega)}]. \quad (32)$$

In Fig. 12, we analyze how much Gaussian random noise of unit variance contributes to the two-sided Laplace transform as a function of the frequency ω for the synthetic UEG model at conditions characterized by $r_s = 2$, $\Theta = 1$, and with a wave number of $q = q_F$, convolved with a Gaussian probe function of width $\sigma = 3.33$ eV; the shaded gray area depicts the corresponding $1\sigma_\Delta$ interval determined by $\sqrt{I(\mathbf{q}, \omega)}$. Figure 12(a) was obtained for $\tau = 0$, where most contributions are due to the positive frequency range. Conversely, Fig. 12(b) corresponds to $\tau = \hbar\beta/2 = \tau_{1/2}$, i.e., the location of the minimum in $\mathcal{L}[S(\mathbf{q}, \omega)]$. In this case, the contribution of the noise to the Laplace transform of the
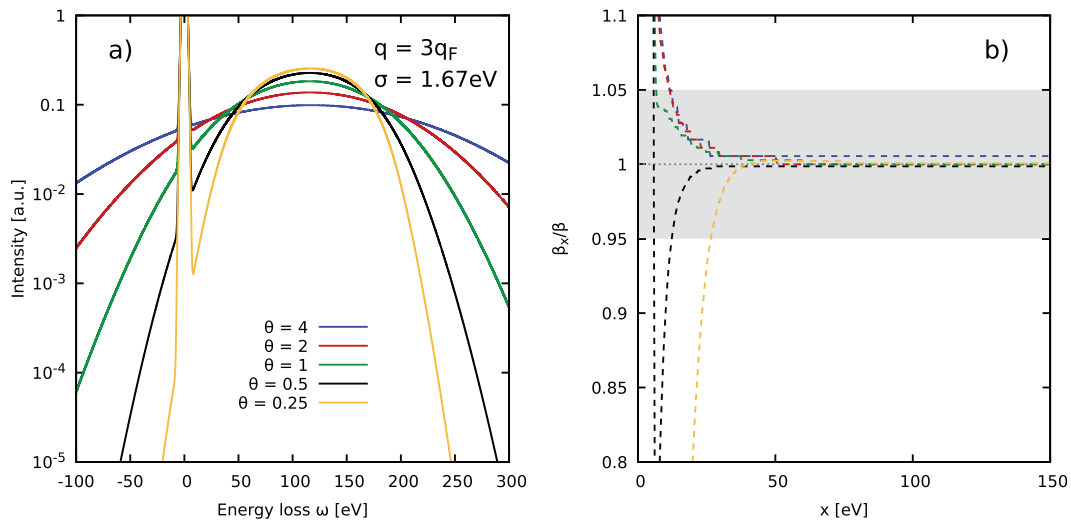

FIG. 11. Influence of the temperature parameter Θ (with $T_F = 12.53$ eV) on the extraction of the temperature at $r_s = 2$ and $q = 3q_F$ with the width of the instrument function $\sigma = 1.67$ eV. (a) Convolved scattering intensity. (b) Convergence of the extracted inverse temperature with the integration boundary x, rescaled by the corresponding exact value of β. The shaded gray area indicates an interval of $\pm 5\%$ and has been included as a reference.
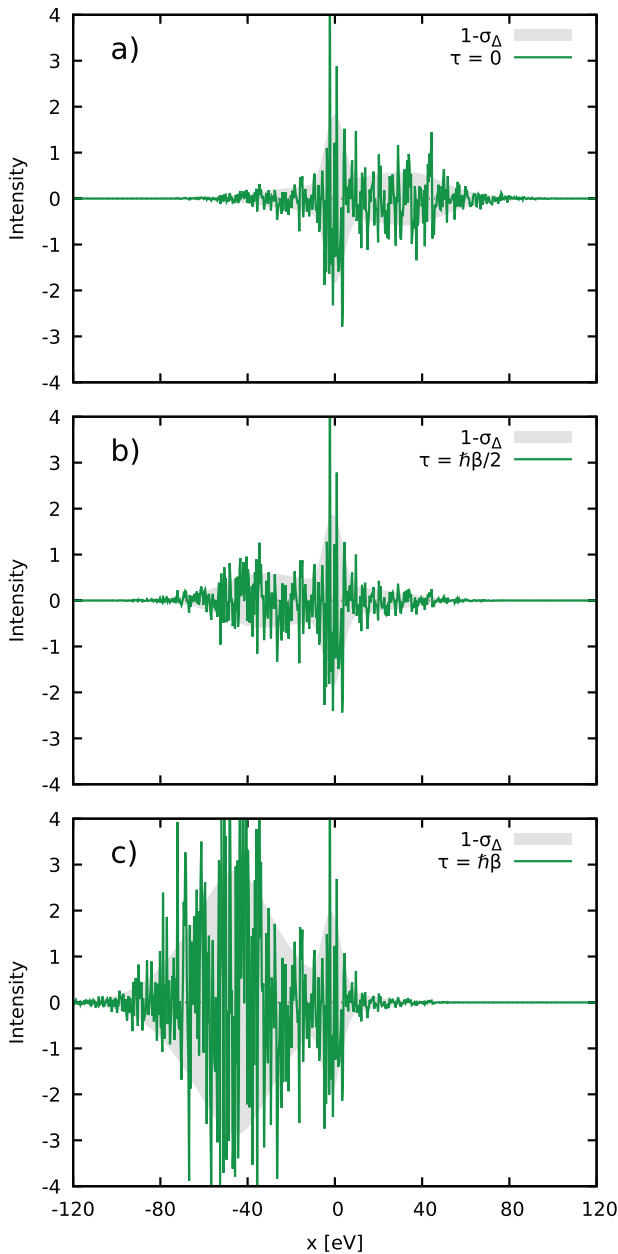
FIG. 12. Frequency-resolved contribution to the Laplace transform of Gaussian random noise of unit variance $\mathcal{L}_x[\xi_1(\omega)\sqrt{I(\mathbf{q},\omega)}]$, see Eq. (32), for a synthetic intensity from the UEG with $r_s = 2$, $\Theta = 1$ ($T = 12.53$ eV), and $q = q_F$ convolved with a Gaussian instrument function of width $\sigma = 3.33$ eV. (a) $\tau = 0$, (b) $\tau = \hbar\beta/2$, and (c) $\tau = \hbar\beta$. The shaded gray area depicts the corresponding $1\sigma_\Delta$ interval that is defined by $\sqrt{I(\mathbf{q},\omega)}$.

intensity looks nearly identical to Fig. 12(a) but mirrored at the y-axis. Finally, Fig. 12(c) shows the same information for $\tau = \hbar\beta$. In this case, the noise in the negative frequency range is substantially increased compared to the previous two cases. In practice, it can, thus, be expected that we can resolve $F(\mathbf{q},\tau)$ with higher accuracy in the range of $0 \leq \tau \leq \tau_{1/2}$ compared to $\tau > \tau_{1/2}$.

To illustrate the remarkable robustness of ITCFT with respect to noise in the experimental data, we perturb synthetic intensities with a series of realistic noise of different pre-factors σ_Δ in Fig. 13. The top row was obtained for $\sigma_\Delta = 0.01$, and the intensity itself is shown in Fig. 13(a), with the green and red curves showing the perturbed and exact data, respectively. The extraction of the (inverse) temperature from the location of the minimum in $F(\mathbf{q},\tau)$ is shown in Fig. 13(b), where the shaded gray area indicates an interval of $\pm 5\%$ around the exact value. The solid black line shows the usual convergence with respect to the integration boundary x of the exact intensity, and the dashed blue and green curves have been obtained using two independent sets of random noise. Clearly, both curves attain the correct inverse temperature in the limit of large x despite the perturbation.

An additional question of high practical importance is whether it is possible to quantify the uncertainty in the extracted temperature when the noisy experimental data for the intensity is taken as the only input. This requires the reconstruction of the variance σ_Δ of the Gaussian noise in Eq. (30), which can be reliably accomplished in the following way. First, we compute a smoothed intensity $I_{\text{smooth}}(\mathbf{q},\omega)$ by averaging the experimental signal over a number of adjacent frequency points. The precise number of frequencies and the particular values of the weights are of minor importance for this idea. Then, we compute a set of corresponding noise according to

$$\Delta I_{\text{exp}}(\mathbf{q},\omega) = I_{\text{exp}}(\mathbf{q},\omega) - I_{\text{smooth}}(\mathbf{q},\omega). \quad (33)$$

Initially, we obtain the reconstructed Gaussian noise variable $\xi_{\sigma_\Delta}(\omega)$ as

$$\xi_{\sigma_\Delta}(\omega) = \frac{\Delta I_{\text{exp}}(\mathbf{q},\omega)}{\sqrt{I_{\text{smooth}}(\mathbf{q},\omega)}}. \quad (34)$$

In Fig. 14, we show a histogram of the, thus, reconstructed noise (red bars), which is in excellent agreement with the true distribution $\sigma_\Delta = 0.05$ (depicted in the center row of Fig. 13). In practice, one can then obtain the reconstructed σ_Δ either from a Gaussian fit of the histogram or by evaluating

$$\sigma_\Delta = \left(\frac{1}{M}\sum_{i=0}^{M-1}\xi_{\sigma_\Delta}^2(\omega_i)\right)^{1/2}. \quad (35)$$

To estimate the corresponding uncertainty in $F(\mathbf{q},\tau)$ and, in this way, also in the extracted inverse temperature β, we generate a set of K independent random noise samples from this distribution, resulting in a set of trial functions

$$F_x^\alpha(\mathbf{q},\tau) = \mathcal{L}_x[I_{\text{exp}}(\mathbf{q},\omega)] + \mathcal{L}_x\left[\xi_{\sigma_\Delta}^\alpha(\omega)\sqrt{I_{\text{smooth}}(\mathbf{q},\omega)}\right] \quad (36)$$

with $\alpha = 0, \ldots, K-1$. From Eq. (36), we can directly estimate the associated variance due to the random noise in the experimental intensity both in the Laplace transform and subsequently in the extracted temperature.

The results for this uncertainty in β (given as the 2σ-interval) are included in Fig. 13 as the shaded red and green areas, which, indeed, give a real measure for the fluctuation around the exact curve. The corresponding results for the Laplace transform $F(\mathbf{q},\tau)$ are shown in Fig. 13(c), where the solid yellow curve shows the exact result. The dashed black curve has been obtained by taking as input the perturbed data
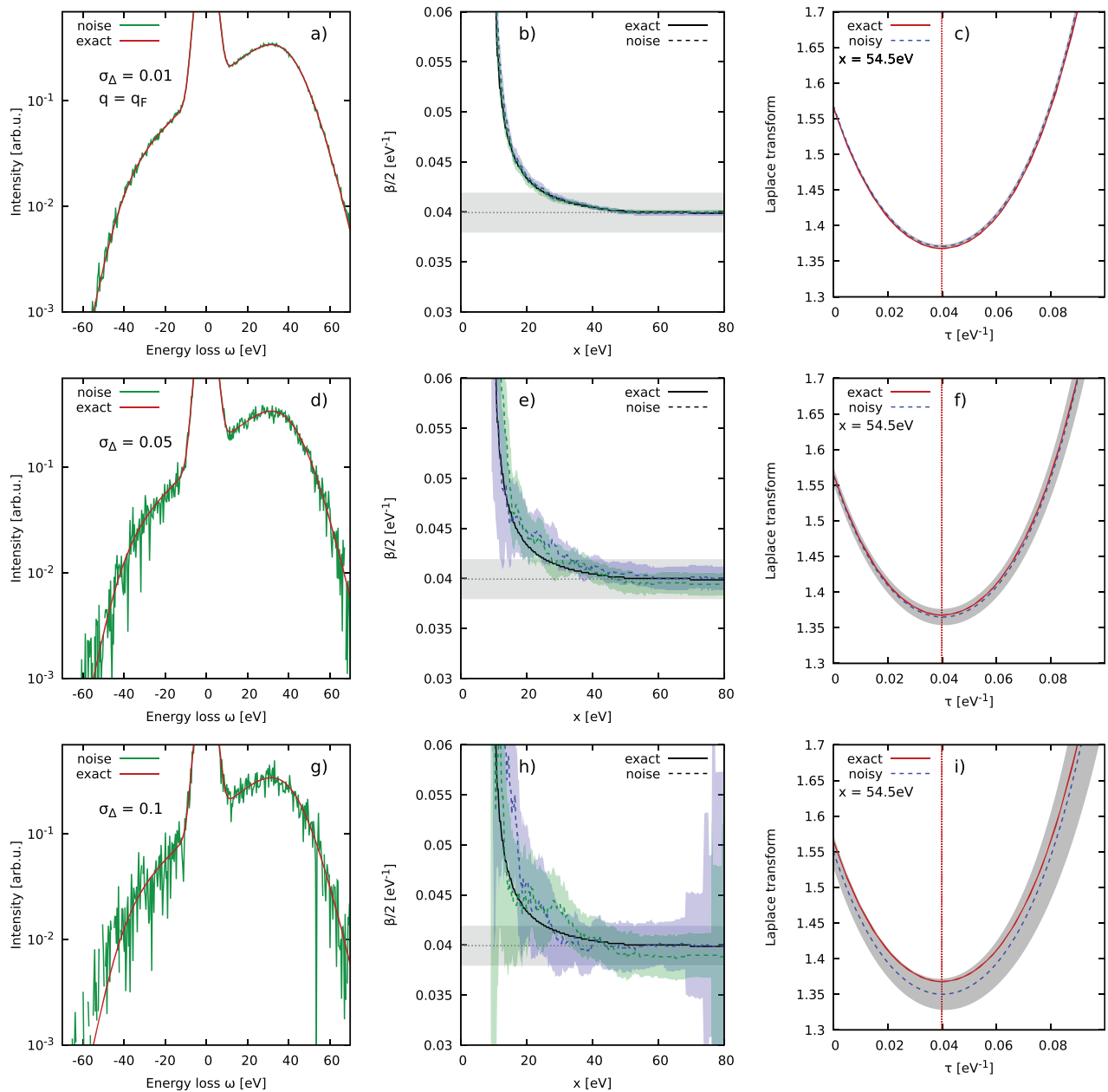
FIG. 13. Temperature extraction of noisy input data for the intensity of a UEG at $r_s = 2$, $\Theta = 1$ ($T = 12.53$ eV), and $q = q_F$ convolved with a Gaussian instrument function of width $\sigma = 3.33$ eV. Left [(a), (d), (g)]: exact (red) and perturbed (green) intensity; center [(b), (e), (h)]: extraction of the temperature with respect to the integration boundary x, with the shaded gray area indicated an interval of $\pm 5\%$ included as a reference; right [(c), (f), (i)]: Laplace transform $F(\mathbf{q}, \tau)$ with corresponding uncertainty obtained from Eq. (36). Top: $\sigma_\Delta = 0.01$, center: $\sigma_\Delta = 0.05$, bottom: $\sigma_\Delta = 0.1$.

and is close to the former, although a small yet significant deviation is observed. The associated uncertainty in $F(\mathbf{q}, \tau)$ computed from Eq. (36) has been included as the shaded gray area and nicely fits the observed difference.

In the center row of Fig. 13, we repeat this analysis for a larger magnitude of the random noise, $\sigma_\Delta = 0.05$. Evidently, the larger noise level is directly propagated into larger fluctuations in the extraction of

the temperature shown in Fig. 13(e). At the same time, we stress that (1) the error bars from Eq. (36) capture these fluctuations very well, and (2) that the extracted temperature is accurate to ~2% despite the substantial noise level in the input data. The imaginary-time intermediate scattering function depicted in Fig. 13(f) exhibits similar behavior.

Finally, we consider an even higher noise level in $\sigma_\Delta = 0.1$ shown in the bottom row of Fig. 13. Still, the extracted temperatures
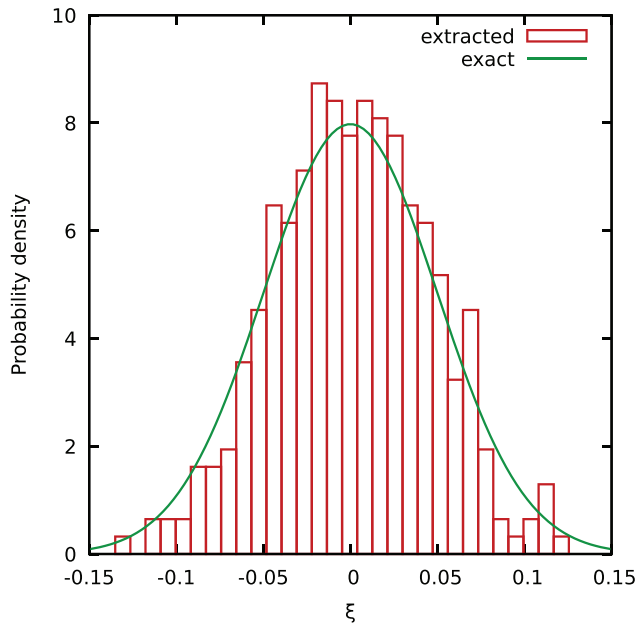
FIG. 14. Red: Reconstructed noise, Eq. (34); green: utilized normal distribution of random noise that has been used to perturb the data in Fig. 13 with $\sigma_\Delta = 0.05$.

remain within $\sim 4\%$ of the exact result, and our estimated uncertainty measures are accurate both for β and $F(\mathbf{q}, \tau)$.

V. APPLICATION OF ITCFT TO ANALYSIS OF EXPERIMENTAL SCATTERING DATA

In Secs. III and IV, we have demonstrated the capability of our new approach for extracting the exact temperature from a scattering intensity signal in different situations. Moreover, we have shown that our method is highly robust with respect to noisy input data and have introduced a framework for the empirical quantification of the associated uncertainty both in the temperature and in the imaginary-time intermediate scattering function $F(\mathbf{q}, \tau)$. In the following, we turn our attention to actual experimentally measured data and reanalyze (1) an experiment on warm dense graphite by Kraus et al.[18] and (2) the pioneering investigation of plasmons in warm dense beryllium by Glenzer et al.[26]

A. Graphite

In Fig. 15, we show our new analysis of the XRTS signal on isochorically heated graphite by Kraus et al.[18] In the left column, we show the measured intensity as the green curve, where accurate data are available over three orders of magnitude. Interestingly, the main source of uncertainty in this experiment is due to the somewhat unclear shape of the instrument function $R(\omega)$. Two plausible possibilities are shown as the blue curves in Figs. 15(a) and 15(d).

From a practical perspective, it is very useful to start the investigation of the experimental dataset by analyzing the distribution of the noise. In Fig. 16(a), we show the corresponding results for Eq. (34) as the red circles, where we have used a smoothening kernel taking into account the nearest five (± 2) frequency bins for each value of ω for the evaluation of Eq. (33). Evidently, the deviations fluctuate around

the origin, and the overall amplitude of $\xi_{\sigma_\Delta}(\omega)$ appears to be approximately constant over the entire ω range. This is a nice empirical validation of the functional form in Eq. (31). For completeness, we note that the elastic feature itself has been omitted from this analysis, as appropriately taking into account the comparably large curvature of $I(\mathbf{q}, \omega)$ in this region would require a separate, adaptive smoothing procedure; this is not needed for accurate quantification of the noise level. In Fig. 15(b), we show the corresponding histogram as the red bars, which can be well reproduced by a Gaussian fit (green curve). Both the fit and the direct evaluation of Eq. (35) give a variance of $\sigma_\Delta \sim 10^{-2}$, which is used to quantify the uncertainty of both the temperature and $F(\mathbf{q}, \tau)$ in the following.

Returning to Figs. 15(b) and 15(d), we find that convergence with the integration boundary x starts around $x = 125$ eV. We note that going beyond $x = 140$ eV does not make sense in practice, as the experimentally measured intensity vanishes within the given noise level for $\omega \lesssim -140$ eV. From these panels, we can clearly see that using either the narrow or the broad instrument function (which we truncate at $\omega = 90$ eV as the constant asymptotes given in the original Ref. 18 are plainly unphysical and would lead to a diverging Laplace transform $\mathcal{L}[R(\omega)]$) has a substantial impact on the extracted temperature. Consequently, we gave our final estimate as $T = 18 \pm 2$ eV in our previous investigation.[25] At the same time, we stress that the resulting uncertainty due to the somewhat unknown $R(\omega)$ is considerably smaller than in the original; Ref. 18, where the applied Chihara fit gave $T = 21$ eV with an uncertainty of $\sim 50\%$.

Finally, we show our estimates for $F_x(\mathbf{q}, \tau) \approx F(\mathbf{q}, \tau)$ for a converged integration boundary of $x = 126.8$ eV in the right column of Fig. 15. In particular, the solid green curves show our direct evaluation of Eq. (23), and the shaded gray area indicates the corresponding uncertainty interval. In addition, we also mirror this function around $\tau_{1/2}$ (which is estimated from the minimum in the green curve), i.e., $F(\mathbf{q}, \hbar\beta - \tau)$, and the results are shown as the dashed red curve, with the shaded red area indicating the correspondingly mirrored uncertainty interval. Evidently, our extracted results for $F(\mathbf{q}, \tau)$ are fairly symmetric within the given uncertainty range for both instrument functions, although the degree of asymmetry [i.e., the difference between $F(\mathbf{q}, \tau)$ and $F(\mathbf{q}, \hbar\beta - \tau)$] is somewhat smaller for the narrower instrument function (top). Finally, the dotted blue curves show the two-sided Laplace transformation of the respective $R(\omega)$. Clearly, the impact of the latter is more pronounced for the broader instrument function, as expected.

In conclusion, our present analysis agrees with the less well-controlled Chihara model-based analysis in the original Ref. 18 and highlights the importance of accurate characterization of the instrument function in future scattering experiments.

B. Beryllium

The second experimental dataset that we reanalyze in the present work is the scattering experiment focusing on the plasmons in warm dense beryllium shown in Fig. 17. Panel (a) shows the experimentally measured XRTS intensity as the green curve, which is clearly afflicted with a much larger noise level compared to the graphite data that we have considered previously. The corresponding reconstruction of the error distribution is shown in Fig. 18, where we find again good agreement with the functional form of Eq. (31); the few outliers for $\omega < 0$ are possibly an artifact from a nearly vanishing intensity signal for
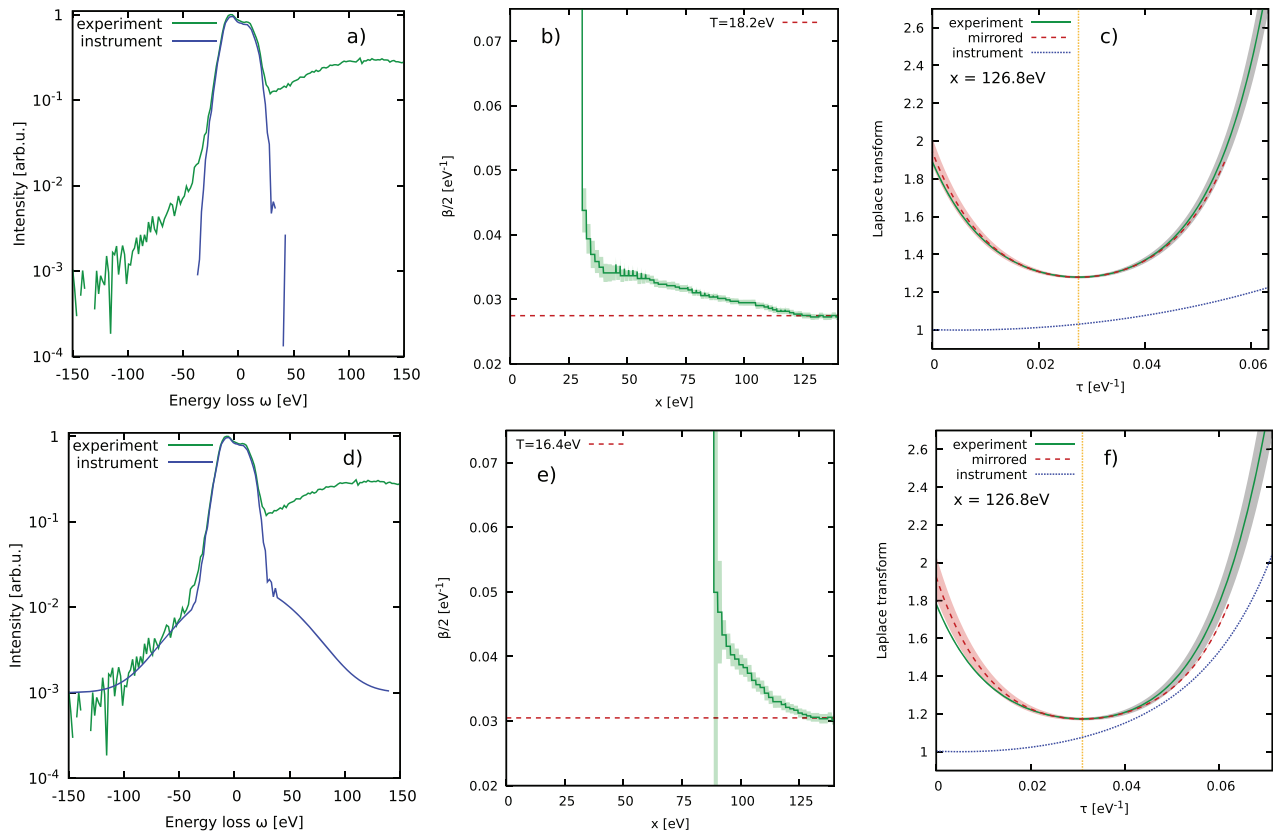
FIG. 15. Analysis of the graphite data collected by Kraus *et al.*[18] for two possible instrument functions (top and bottom row). Left [(a) and (d)]: experimental XRTS intensity (green) and instrument function (blue); center [(b) and (e)]: extraction of the temperature with respect to the integration boundary x; right [(c) and (f)]: $F_x(\mathbf{q}, \tau)$ for $x = 126.8\,\text{eV}$.
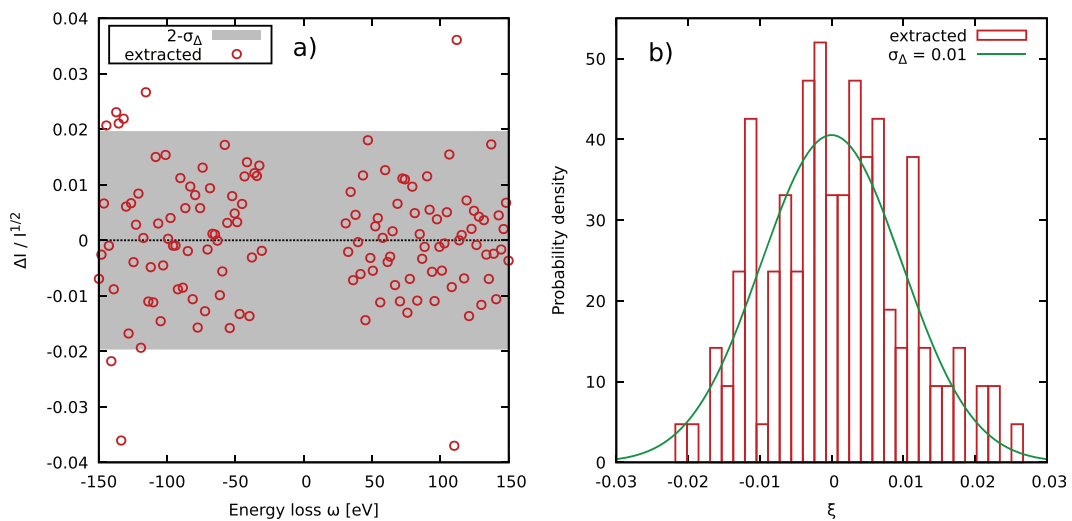

FIG. 16. Error analysis of graphite data by Kraus *et al.*[18] shown in Fig. 15. (a) Rescaled deviation between data and smoothened function and (b) corresponding histogram.
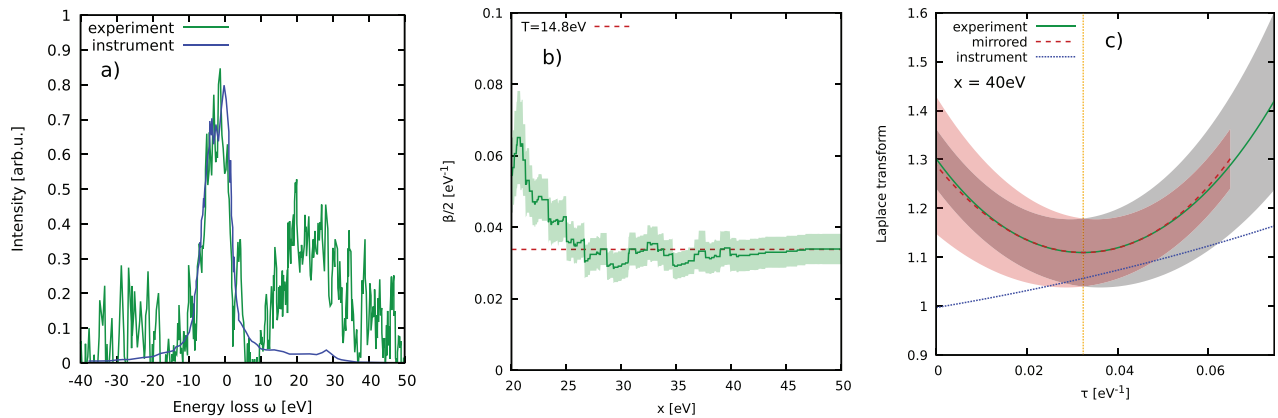
FIG. 17. Temperature analysis of beryllium data by Glenzer *et al.*[26] (a) Experimental XRTS intensity (green) and instrument function (blue); (b) extraction of the temperature with respect to the integration boundary x; (c) $F_x(\mathbf{q}, \tau)$ for $x = 40$ eV.

some ω, leading to increased values for $\Delta I(\mathbf{q}, \omega)/\sqrt{I(\mathbf{q}, \omega)}$ or due to the approximate nature of Eq. (31). We have used the same smoothening kernel to evaluate Eq. (33) as for Fig. 16. Figure 18 shows the corresponding histogram of $\xi_{\sigma_\Delta}(\omega)$ as the red bars, which is accurately reproduced by a Gaussian fit with a variance of $\sigma_\Delta = 0.21$ (green curve). Note that we omit the outliers with an intensity below an empirical threshold of $I_{\min} = 10^4$.

The reconstructed distribution of the random noise is again used to empirically quantify the uncertainty. In Fig. 17(b), we show the convergence of the extracted (inverse) temperature with the integration boundary x, and the shaded gray uncertainty interval very plausibly fits the observed noise in the green curve. As a final result, we obtain a temperature of $T = 14.8 \pm 2$ eV. This is close to the value of $T = 12$ eV given in the original Ref. 26, which was obtained from an approximate Mermin model.[87] In the context of the present work, the main point of Fig. 17(b) is the remarkable robustness of our methodology even with respect to the considerable noise level in experimental

data. Finally, we show our extracted imaginary-time intermediate scattering function in Fig. 17(c). Evidently, the direct evaluation of Eq. (23) (solid green) is in nearly perfect agreement with the mirrored curve (dashed red) over the entire τ-range despite the given uncertainty range (shaded areas).

VI. SUMMARY AND OUTOOK

In this work, we have given a detailed introduction to our new, model-free methodology for extracting the temperature of arbitrary complex materials from XRTS measurements,[25] referred to as imaginary-time correlation function thermometry (ITCFT). In particular, we have presented an extensive analysis of synthetic scattering spectra over a wide range of wave numbers and temperatures. Evidently, the method works exceptionally well covering the range from the collective to the single-particle regimes. In addition, we have studied the impact of the width of the instrument function, which decisively determines the minimum temperature that can be extracted
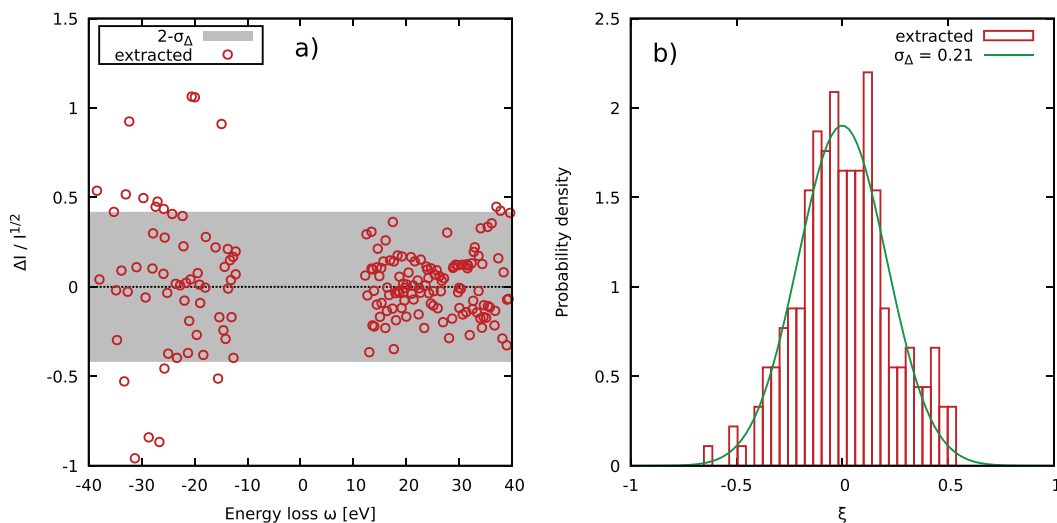

FIG. 18. Error analysis of beryllium data by Glenzer *et al.*[26] shown in Fig. 17. (a) Rescaled deviation between data and smoothened function and (b) corresponding histogram.

from a corresponding XRTS signal. Naturally, these findings have direct implications for the design of future experimental XRTS setups.

Furthermore, we have introduced an empirical framework for quantifying the impact of experimental noise both on the extracted temperature and on $F(\mathbf{q}, \tau)$ itself. In practice, the method is well-behaved and highly robust even against substantial noise levels. As a practical demonstration, we have reanalyzed the XRTS experiments by Kraus et al.[18] and Glenzer et al.[26]

On the strength of the analysis presented throughout this paper, we believe that our new ITCFT technique will have a considerable impact on a gamut of applications related to the study of WDM, including the highly active fields of inertial confinement fusion[9,10] and laboratory astrophysics.[88] On the one hand, we note that our method is particularly suited for modern x-ray free electron laser facilities with a high repetition rate such as LCLS,[48] SACLA,[49] and the European XFEL.[47,89] Specifically, its negligible computational cost will open up unprecedented possibilities for the on-the-fly interpretation of XRTS experiments. On the other hand, the robustness with respect to noise makes our approach also the method of choice for less advanced laser diagnostics at other facilities such as NIF.[90]

Future developments might include a more rigorous analysis on the impact potential uncertainties in the characterization of the instrument function have on the extracted temperature. Similarly, possible effects of the background subtraction need to be investigated. Extending our framework to take into account the spatial inhomogeneity of a sample such as the fuel capsule in an ICF experiment[41,54] seems promising. Finally, we note that $F(\mathbf{q}, \tau)$ contains the same information as $S(\mathbf{q}, \omega)$ and, therefore, can be used to extract physical information beyond the temperature such as quasi-particle excitation energies or even more complicated phenomena such as the roton feature[32] in the strongly coupled electron liquid.[28]

AUTHOR DECLARATIONS
Conflict of Interest

The authors have no conflicts to disclose.

Author Contributions

Tobias Dornheim: Conceptualization (lead); Investigation (lead); Methodology (lead); Writing – original draft (lead); Writing – review & editing (lead). **Jan Vorberger:** Methodology (equal); Writing – original draft (equal); Writing – review & editing (equal). **Maximilian Böhme:** Methodology (equal); Writing – review & editing (equal). **Dave A. Chapman:** Investigation (supporting); Methodology (supporting); Writing – original draft (equal); Writing – review & editing (equal). **Dominik Kraus:** Writing – original draft (equal); Writing – review & editing (equal). **Thomas Robert Preston:** Writing – original draft (equal); Writing – review & editing (equal). **Zhandos Moldabekov:** Writing – review & editing (equal). **Niclas Schlünzen:** Writing – review & editing (equal). **Attila Cangi:** Writing – review & editing (equal). **Tilo Doeppner:** Writing – review & editing (equal).

DATA AVAILABILITY

The data that support the findings of this study are available from the corresponding author upon reasonable request.

APPENDIX A: THE ROLE OF THE GENERALIZED SCATTERING CROSS SECTION IN XRTS EXPERIMENTS

As discussed in Sec. II B 1, the form of the scattered power spectrum depends on the differential Thomson cross section $\partial\tilde{\sigma}/\partial\Omega|_{\mathrm{T}}$. In this expression, the cross section is given a tilde symbol to mark it as a so-called "generalized" cross section. A fact that appears to seldom be addressed in the broader XRTS literature is that there is a subtle distinction between the foregoing expression and that which arises from the Klein–Nishina formula describing the cross section for Compton scattering of a photon from a single, isolated electron. This subject has been discussed extensively and from the perspective of a rigorous quantum-statistical framework by Crowley and Gregori.[37] We mention it here only to further emphasize their conclusion.

Crowley and Gregori summarize that the form of the cross section appropriate to characterize a scattering experiment crucially depends on the mechanism of how the spectrum is recorded, i.e., using either a "quantum" or "classical" detector. Specifically, a quantum detector is sensitive to the number of individual photons, whereas a classical detector is the one that cares only about the total energy incident upon it (per spectral channel). The crucial difference is that the cross section for scattering from electrons from the perspective of a classical detector introduces an additional factor of ω_s/ω_0, since the energy in a particular spectral channel is proportional to its frequency. The two cross sections are related by

$$d\Sigma = \frac{\omega_s}{\omega_0} d\sigma, \tag{A1}$$

where σ is the quantum cross section and Σ is its classical counterpart. The generalized cross section to be used in Eq. (4) is then

$$\left.\frac{\partial\tilde{\sigma}}{\partial\Omega}\right|_{\mathrm{T}} = \left(\frac{\omega_s}{\omega_0}\right)^n r_e^2 \, G(\theta, \phi). \tag{A2}$$

Here, r_e is the classical electron radius, and the geometrical term $G(\theta, \phi) = (\hat{\mathbf{e}}_0 \cdot \hat{\mathbf{e}}_s)^2$ gives the projection of the unit vectors for the incident and scattered x-ray polarizations.[17] The quantum case ($\tilde{\sigma} \to \sigma$) corresponds to $n = 1$ and the classical case ($\tilde{\sigma} \to \Sigma$) to $n = 2$. Accordingly, for spectra that span a large dynamic range, a classical detector will observe a marginally different shape to the scattered power spectrum due to this additional factor, which, in the most general case, can distort the results inferred from forward

modeling. Since most major facilities at which XRTS is currently deployed utilize detectors which record only the magnitude of the scattered intensity per pixel, we assume throughout this work that $n = 2$. Fortunately, this consideration can mostly be ignored for high-energy x-ray probes (see Appendix B), such as those produced by the new generation of XFEL facilities.

APPENDIX B: DERIVING THE APPROXIMATE FORM OF THE WAVE NUMBER SHIFT

It is well known that the evaluation of the dynamic properties of matter in which the particle distribution functions are isotropic in momentum space requires only the magnitude of the momentum shift variable $q = |\mathbf{q}|$. In the context of XRTS, momentum conservation within the scattering process gives the shift in the wave vector as $\mathbf{q} = \mathbf{q}_0 - \mathbf{q}_s$. The magnitude then immediately follows from application of the cosine formula,

$$|\mathbf{q}| \equiv q(q_0, q_s, \theta) = \left(q_0^2 + q_s^2 - 2q_0 q_s \cos\theta\right)^{1/2}, \quad \text{(B1)}$$

in which $\theta = \angle(\mathbf{q}_0, \mathbf{q}_s)$ is the scattering angle defined in Fig. 1. In the case where electromagnetic dispersion can be ignored, i.e., for target electron densities far below the critical density $n_e \ll n_{\text{crit}}(\omega) = \varepsilon_0 m_e \omega^2/e^2$, one may write the relationship between frequency and wave number as $\omega = cq$, such that Eq. (B1) becomes

$$q(\omega_0, \omega, \theta) = \frac{\omega_0}{c}\left(1 + \tilde{\omega}^2 - 2\tilde{\omega}\cos\theta\right)^{1/2}, \quad \text{(B2)}$$

where $\tilde{\omega} = \omega_s/\omega_0$. From the consummate energy conservation, $\omega = \omega_0 - \omega_s$, one has $\tilde{\omega} = (1 - \omega/\omega_0)$. For XRTS, the energy of the probe, $E_0 = \hbar\omega_0$, is sufficiently high that the spectral features of the scattered spectrum occupy a dynamic range that strongly fulfills the condition $|\omega|/\omega_0 \ll 1$ and, thus, we have both $\tilde{\omega} \approx 1$ and

$$q(\omega_0, \omega, \theta) \approx \frac{\omega_0}{c}\left[2(1 - \cos\theta)\right]^{1/2} = \frac{\omega_0}{c}\left[4\sin^2(\theta/2)\right]^{1/2}$$
$$= \frac{2\omega_0}{c}\sin(\theta/2) \equiv q_{\text{approx}}(\omega_0, \theta), \quad \text{(B3)}$$

which is the well-known approximate form used throughout the analysis of XRTS experiments. The fact that this relationship is only approximate and is not appropriate for all scattering experiments is well known in the optical Thomson scattering (OTS) community; it is essential to account for the change in q across the spectral range in order to capture the change in the Landau damping rate on the red- and blue-shifted plasmon resonances,[91] which strongly influence forward data fitting results. On the contrary, this is seldom discussed in the context of XRTS data analysis.

Note also that the other dynamic term in the definition of the scattered power spectrum Eq. (6) can, and, indeed, should be similarly approximated as unity. These consistent simplifications allow the usage of the spectral two-sided Laplace transform of the reduced intensity $I(\mathbf{q}, \omega)$ at constant $\mathbf{q}$ and further enable the latter to be robustly taken to be interpreted as the convolution defined in Eq. (10).

The restriction that the approximate form of q must be well-fulfilled in order to properly use the Laplace transform indicates that further work must be undertaken in order to use the

temperature diagnostic described herein on systems where the full expression is required, such as OTS experiments.

APPENDIX C: INVARIANCE OF THE TWO-SIDED LAPLACE TRANSFORM WITH RESPECT TO A FREQUENCY SHIFT ω_0

The combined source and instrument function of an XRTS experiment has a global maximum around an energy shift ω_0, which is either determined by the XFEL energy[17] or a backlighter emission spectrum.[51] Similarly, the measured intensity, too, will be centered around the same ω_0. In practice, it might, however, not be easily possible to unambiguously resolve ω_0, e.g., due to the inevitable experimental noise. Here, we briefly demonstrate that the extracted ITCF $F(\mathbf{q}, \tau)$ is, in fact, invariant with respect to ω_0. Let $\bar{R}(\omega) = R(\omega - \omega_0)$ denotes a shifted source and instrument function that is centered around $\omega = 0$, and $\bar{I}(\omega)$ the equally shifted intensity; the dynamic structure factor $S(\omega)$ is always centered around $\omega = 0$, and the wave number q is dropped from the following considerations for simplicity.

The two-sided Laplace transform of $\bar{R}(\omega)$ is given by

$$\mathcal{L}[\bar{R}(\omega)] = \int_{-\infty}^{\infty} d\omega\, e^{-\tau\omega}\bar{R}(\omega)$$
$$= \int_{-\infty}^{\infty} d\omega\, e^{-\tau(\omega - \omega_0)}R(\omega)$$
$$= e^{\omega_0\tau}\mathcal{L}[R(\omega)], \quad \text{(C1)}$$

where the second line has been obtained by inserting $R(\omega)$ and shifting the integration variable by $\omega \to \omega - \omega_0$. Similarly, we find for the convolved XRTS intensity

$$L(\omega) \equiv \mathcal{L}[\bar{R}(\omega) \circledast S(\omega)]$$
$$= \int_{-\infty}^{\infty} d\omega\, e^{-\tau\omega} \int_{-\infty}^{\infty} d\Omega\, S(\Omega)\bar{R}(\omega - \Omega)$$
$$= \int_{-\infty}^{\infty} d\Omega\, S(\Omega) \int_{-\infty}^{\infty} d\omega\, e^{-\tau(\omega - \omega_0)}R(\omega - \Omega)$$
$$= e^{\tau\omega_0}\mathcal{L}[R(\omega) \circledast S(\omega)]. \quad \text{(C2)}$$

Clearly, the exponential pre-factors in the last lines of Eqs. (C1) and (C2) cancel when being inserted into Eq. (20), which means that $F(\mathbf{q}, \tau)$ is invariant with respect to a frequency shift by ω_0.

APPENDIX D: SYNTHETIC DATA FOR THE DYNAMIC STRUCTURE FACTOR

To compute the UEG model $S_{\text{UEG}}(\mathbf{q}, \omega)$ for the synthetic data [cf. Eq. (25)], we utilize the dynamic linear density response function,[52,92]

$$\chi_{\text{UEG}}(\mathbf{q}, \omega) = \frac{\chi_0(\mathbf{q}, \omega)}{1 - V_{ee}(q)[1 - G(\mathbf{q}, \omega)]\chi_0(\mathbf{q}, \omega)}, \quad \text{(D1)}$$

with $V_{ee}(q) = e^2/\epsilon_0 q^2$ ($= 4\pi/q^2$ in HAU) denoting the Fourier transform of the bare electron–electron Coulomb interaction and $\chi_0(\mathbf{q}, \omega)$ being the dynamic density–density response function of a uniform ideal Fermi gas (often called the Lindhard response

function). The dynamic local field correction $G(\mathbf{q}, \omega)$ then contains the complete information about electronic exchange–correlation effects, setting $G(\mathbf{q}, \omega) \equiv 0$ in Eq. (D1) leads to a description of the density response on a mean-field level, which is commonly referred to as the random phase approximation. The connection between $\chi(\mathbf{q}, \omega)$ and the DSF is given by the fluctuation–dissipation theorem:

$$S_{\text{UEG}}(\mathbf{q}, \omega) = \frac{\hbar}{\pi n_e} \frac{\text{Im}\{\chi_{\text{UEG}}(\mathbf{q}, \omega)\}}{1 - e^{-\beta\hbar\omega}} . \tag{D2}$$

While the full $G(\mathbf{q}, \omega)$ is generally unknown, it has recently been reported[75,76] that the dependence of the local field correction on the frequency ω can be neglected at metallic densities $G(\mathbf{q}, \omega) \approx G(\mathbf{q}, 0)$; this is certainly true for the value of $r_s = 2$ considered in the present work.

In practice, we use the neural-net representation of the static local field correction $G(\mathbf{q}, 0; r_s, \Theta)$ from Ref. 80 (see Ref. 109 therein for a link to the corresponding repository) to obtain the synthetic UEG results via Eqs. (D1) and (D2).

REFERENCES

[1] V. E. Fortov, "Extreme states of matter on Earth and in space," Phys.-Usp. **52**, 615–647 (2009).

[2] S. Brygoo, P. Loubeyre, M. Millot, J. R. Rygg, P. M. Celliers, J. H. Eggert, R. Jeanloz, and G. W. Collins, "Evidence of hydrogen-helium immiscibility at Jupiter-interior conditions," Nature **593**, 517–521 (2021).

[3] R. G. Kraus, R. J. Hemley, S. J. Ali, J. L. Belof, L. X. Benedict, J. Bernier, D. Braun, R. E. Cohen, G. W. Collins, F. Coppari, M. P. Desjarlais, D. Fratanduono, S. Hamel, A. Krygier, A. Lazicki, J. Mcnaney, M. Millot, P. C. Myint, M. G. Newman, J. R. Rygg, D. M. Sterbentz, S. T. Stewart, L. Stixrude, D. C. Swift, C. Wehrenberg, and J. H. Eggert, "Measuring the melting curve of iron at super-Earth core conditions," Science **375**, 202–205 (2022).

[4] Z. He, M. Rödel, J. Lütgert, A. Bergermann, M. Bethkenhagen, D. Chekrygina, T. E. Cowan, A. Descamps, M. French, E. Galtier, A. E. Gleason, G. F. Glenn, S. H. Glenzer, Y. Inubushi, N. J. Hartley, J.-A. Hernandez, B. Heuser, O. S. Humphries, N. Kamimura, K. Katagiri, D. Khaghani, H. J. Lee, E. E. McBride, K. Miyanishi, B. Nagler, B. Ofori-Okai, N. Ozaki, S. Pandolfi, C. Qu, D. Ranjan, R. Redmer, C. Schoenwaelder, A. K. Schuster, M. G. Stevenson, K. Sueda, T. Togashi, T. Vinci, K. Voigt, J. Vorberger, M. Yabashi, T. Yabuuchi, L. M. V. Zinta, A. Ravasio, and D. Kraus, "Diamond formation kinetics in shock-compressed C-H-O samples recorded by small-angle x-ray scattering and x-ray diffraction," Sci. Adv. **8**, eabo0617 (2022).

[5] A. Benuzzi-Mounaix, S. Mazevet, A. Ravasio, T. Vinci, A. Denoeud, M. Koenig, N. Amadou, E. Brambrink, F. Festa, A. Levy, M. Harmand, S. Brygoo, G. Huser, V. Recoules, J. Bouchet, G. Morard, F. Guyot, T. de Resseguier, K. Myanishi, N. Ozaki, F. Dorchies, J. Gaudin, P. M. Leguay, O. Peyrusse, O. Henry, D. Raffestin, S. L. Pape, R. Smith, and R. Musella, "Progress in warm dense matter study with applications to planetology," Phys. Scr. **2014**, 014060.

[6] B. Militzer, W. B. Hubbard, J. Vorberger, I. Tamblyn, and S. A. Bonev, "A massive core in Jupiter predicted from first-principles simulations," Astrophys. J. **688**, L45–L48 (2008).

[7] D. Saumon, W. B. Hubbard, G. Chabrier, and H. M. van Horn, "The role of the molecular-metallic transition of hydrogen in the evolution of Jupiter, Saturn, and brown dwarfs," Astrophys. J. **391**, 827–831 (1992).

[8] A. Becker, W. Lorenzen, J. J. Fortney, N. Nettelmann, M. Schöttler, and R. Redmer, "*Ab initio* equations of state for hydrogen (H-REOS.3) and helium (He-REOS.3) and their implications for the interior of brown dwarfs," Astrophys. J. Suppl. Ser. **215**, 21 (2014).

[9] R. Betti and O. A. Hurricane, "Inertial-confinement fusion with lasers," Nat. Phys. **12**, 435–448 (2016).

[10] A. B. Zylstra, O. A. Hurricane, D. A. Callahan, A. L. Kritcher, J. E. Ralph, H. F. Robey, J. S. Ross, C. V. Young, K. L. Baker, D. T. Casey, T. Döppner, L. Divol, M. Hohenberger, S. L. Pape, A. Pak, P. K. Patel, R. Tommasini, S. J. Ali, P. A. Amendt, L. J. Atherton, B. Bachmann, D. Bailey, L. R. Benedetti, L. B. Hopkins, R. Betti, S. D. Bhandarkar, J. Biener, R. M. Bionta, N. W. Birge, E. J. Bond, D. K. Bradley, T. Braun, T. M. Briggs, M. W. Bruhn, P. M. Celliers, B. Chang, T. Chapman, H. Chen, C. Choate, A. R. Christopherson, D. S. Clark, J. W. Crippen, E. L. Dewald, T. R. Dittrich, M. J. Edwards, W. A. Farmer, J. E. Field, D. Fittinghoff, J. Frenje, J. Gaffney, M. G. Johnson, S. H. Glenzer, G. P. Grim, S. Haan, K. D. Hahn, G. N. Hall, B. A. Hammel, J. Harte, E. Hartouni, J. E. Heebner, V. J. Hernandez, H. Herrmann, M. C. Herrmann, D. E. Hinkel, D. D. Ho, J. P. Holder, W. W. Hsing, H. Huang, K. D. Humbird, L. Izumi, L. C. Jarrott, J. Jeet, O. Jones, G. D. Kerbel, S. M. Kerr, S. F. Khan, J. Kilkenny, Y. Kim, H. G. Kleinrath, V. G. Kleinrath, C. Kong, J. M. Koning, J. J. Kroll, M. K. G. Kruse, B. Kustowski, O. L. Landen, S. Langer, D. Larson, N. C. Lemos, J. D. Lindl, T. Ma, M. J. MacDonald, B. J. MacGowan, A. J. Mackinnon, S. A. MacLaren, A. G. MacPhee, M. M. Marinak, D. A. Mariscal, E. V. Marley, L. Masse, K. Meaney, N. B. Meezan, P. A. Michel, M. Millot, J. L. Milovich, J. D. Moody, A. S. Moore, J. W. Morton, T. Murphy, K. Newman, J.-M. G. Di Nicola, A. Nikroo, R. Nora, M. V. Patel, L. J. Pelz, J. L. Peterson, Y. Ping, B. B. Pollock, M. Ratledge, N. G. Rice, H. Rinderknecht, M. Rosen, M. S. Rubery, J. D. Salmonson, J. Sater, S. Schiaffino, D. J. Schlossberg, M. B. Schneider, C. R. Schroeder, H. A. Scott, S. M. Sepke, K. Sequoia, M. W. Sherlock, S. Shin, V. A. Smalyuk, B. K. Spears, P. T. Springer, M. Stadermann, S. Stoupin, D. J. Strozzi, L. J. Suter, C. A. Thomas, R. P. J. Town, E. R. Tubman, P. L. Volegov, C. R. Weber, K. Widmann, C. Wild, C. H. Wilde, B. M. Van Wonterghem, D. T. Woods, B. N. Woodworth, M. Yamaguchi, S. T. Yang, and G. B. Zimmerman, "Burning plasma achieved in inertial fusion," Nature **601**, 542–548 (2022).

[11] S. X. Hu, B. Militzer, V. N. Goncharov, and S. Skupsky, "First-principles equation-of-state table of deuterium for inertial confinement fusion applications," Phys. Rev. B **84**, 224109 (2011).

[12] A. Lazicki, D. McGonegle, J. R. Rygg, D. G. Braun, D. C. Swift, M. G. Gorman, R. F. Smith, P. G. Heighway, A. Higginbotham, M. J. Suggit, D. E. Fratanduono, F. Coppari, C. E. Wehrenberg, R. G. Kraus, D. Erskine, J. V. Bernier, J. M. McNaney, R. E. Rudd, G. W. Collins, J. H. Eggert, and J. S. Wark, "Metastability of diamond ramp-compressed to 2 terapascals," Nature **589**, 532–535 (2021).

[13] D. Kraus, A. Ravasio, M. Gauthier, D. O. Gericke, J. Vorberger, S. Frydrych, J. Helfrich, L. B. Fletcher, G. Schaumann, B. Nagler, B. Barbrel, B. Bachmann, E. J. Gamboa, S. Göde, E. Granados, G. Gregori, H. J. Lee, P. Neumayer, W. Schumaker, T. Döppner, R. W. Falcone, S. H. Glenzer, and M. Roth, "Nanosecond formation of diamond and lonsdaleite by shock compression of graphite," Nat. Commun. **7**, 10970 (2016).

[14] D. Kraus, J. Vorberger, A. Pak, N. J. Hartley, L. B. Fletcher, S. Frydrych, E. Galtier, E. J. Gamboa, D. O. Gericke, S. H. Glenzer, E. Granados, M. J. MacDonald, A. J. MacKinnon, E. E. McBride, I. Nam, P. Neumayer, M. Roth, A. M. Saunders, A. K. Schuster, P. Sun, T. van Driel, T. Döppner, and R. W. Falcone, "Formation of diamonds in laser-compressed hydrocarbons at planetary interior conditions," Nat. Astron. **1**, 606–611 (2017).

[15] M. L. Brongersma, N. J. Halas, and P. Nordlander, "Plasmon-induced hot carrier science and technology," Nat. Nanotechnol. **10**, 25–34 (2015).

[16] K. Falk, "Experimental methods for warm dense matter research," High Power Laser Sci. Eng. **6**, e59 (2018).

[17] S. H. Glenzer and R. Redmer, "X-ray Thomson scattering in high energy density plasmas," Rev. Mod. Phys. **81**, 1625 (2009).

[18] D. Kraus, B. Bachmann, B. Barbrel, R. W. Falcone, L. B. Fletcher, S. Frydrych, E. J. Gamboa, M. Gauthier, D. O. Gericke, S. H. Glenzer, S. Göde, E. Granados, N. J. Hartley, J. Helfrich, H. J. Lee, B. Nagler, A. Ravasio, W. Schumaker, J. Vorberger, and T. Döppner, "Characterizing the ionization potential depression in dense carbon plasmas with high-precision spectrally resolved x-ray scattering," Plasma Phys. Control Fusion **61**, 014015 (2019).

[19] G. Gregori, S. H. Glenzer, W. Rozmus, R. W. Lee, and O. L. Landen, "Theoretical model of x-ray scattering as a dense matter probe," Phys. Rev. E **67**, 026412 (2003).

[20] K. Falk, E. J. Gamboa, G. Kagan, D. S. Montgomery, B. Srinivasan, P. Tzeferacos, and J. F. Benage, "Equation of state measurements of warm dense

carbon using laser-driven shock and release technique," Phys. Rev. Lett. **112**, 155003 (2014).

[21]*Frontiers and Challenges in Warm Dense Matter*, edited by F. Graziani, M. P. Desjarlais, R. Redmer, and S. B. Trickey (Springer International Publishing, 2014).

[22]M. Bonitz, T. Dornheim, Z. A. Moldabekov, S. Zhang, P. Hamann, H. Kählert, A. Filinov, K. Ramakrishna, and J. Vorberger, "*Ab initio* simulation of warm dense matter," Phys. Plasmas **27**, 042710 (2020).

[23]T. Dornheim, Z. A. Moldabekov, K. Ramakrishna, P. Tolias, A. D. Baczewski, D. Kraus, T. R. Preston, D. A. Chapman, M. P. Böhme, T. Döppner, F. Graziani, M. Bonitz, A. Cangi, and J. Vorberger, "Electronic density response of warm dense matter," Phys. Plasmas **30**, 032705 (2023).

[24]J. Chihara, "Difference in x-ray scattering between metallic and non-metallic liquids due to conduction electrons," J. Phys. F **17**, 295–304 (1987).

[25]T. Dornheim, M. Böhme, D. Kraus, T. Döppner, T. R. Preston, Z. A. Moldabekov, and J. Vorberger, "Accurate temperature diagnostics for matter under extreme conditions," Nat. Commun. **13**, 7911 (2022).

[26]S. H. Glenzer, O. L. Landen, P. Neumayer, R. W. Lee, K. Widmann, S. W. Pollaine, R. J. Wallace, G. Gregori, A. Höll, T. Bornath, R. Thiele, V. Schwarz, W.-D. Kraeft, and R. Redmer, "Observations of plasmons in warm dense matter," Phys. Rev. Lett. **98**, 065002 (2007).

[27]P. Sperling, E. J. Gamboa, H. J. Lee, H. K. Chung, E. Galtier, Y. Omarbakiyeva, H. Reinholz, G. Röpke, U. Zastrau, J. Hastings, L. B. Fletcher, and S. H. Glenzer, "Free-electron x-ray laser measurements of collisional-damped plasmons in isochorically heated warm dense matter," Phys. Rev. Lett. **115**, 115001 (2015).

[28]T. Dornheim, Z. Moldabekov, P. Tolias, M. Böhme, and J. Vorberger, "Physical insights from imaginary-time density–density correlation functions," arXiv:2209.02254 (2022).

[29]T. Dornheim, J. Vorberger, Z. Moldabekov, and M. Böhme, "Analyzing X-ray Thomson scattering experiments of warm dense matter in the imaginary-time domain: Theoretical models and simulations," arXiv:2211.00579 (2022).

[30]H. Kleinert, *Path Integrals in Quantum Mechanics, Statistics, Polymer Physics, and Financial Markets*, 5th ed. (World Scientific, 2009).

[31]D. Thirumalai and B. J. Berne, "On the calculation of time correlation functions in quantum systems: Path integral techniques," J. Chem. Phys. **79**, 5029–5033 (1983).

[32]T. Dornheim, Z. Moldabekov, J. Vorberger, H. Kählert, and M. Bonitz, "Electronic pair alignment and roton feature in the warm dense electron gas," Commun. Phys. **5**, 304 (2022).

[33]T. Dornheim, Z. A. Moldabekov, and J. Vorberger, "Nonlinear density response from imaginary-time correlation functions: *Ab initio* path integral Monte Carlo simulations of the warm dense electron gas," J. Chem. Phys. **155**, 054110 (2021).

[34]M. F. Herman, E. J. Bruskin, and B. J. Berne, "On path integral Monte Carlo simulations," J. Chem. Phys. **76**, 5150–5155 (1982).

[35]T. Ott, H. Thomsen, J. W. Abraham, T. Dornheim, and M. Bonitz, "Recent progress in the theory and simulation of strongly correlated plasmas: Phase transitions, transport, quantum, and magnetic field effects," Eur. Phys. J. D **72**, 84 (2018).

[36]C. Fortmann, R. Redmer, H. Reinholz, G. Röpke, A. Wierling, and W. Rozmus, "Bremsstrahlung vs. Thomson scattering in VUV-FEL plasma experiments," High Energy Density Phys. **2**, 57 (2006).

[37]B. J. B. Crowley and G. Gregori, "X-ray scattering in many-particle systems," New J. Phys. **15**, 015014 (2013).

[38]D. Kremp, T. Bornath, M. Schlanges, and W. D. Kraeft, *Quantum Statistics of Nonideal Plasmas*, Springer Series on Atomic, Optical, and Plasma Physics (Springer, Berlin Heidelberg, 2006).

[39]A. Höll, T. Bornath, L. Cao, T. Döppner, S. Düsterer, E. Förster, C. Fortmann, S. H. Glenzer, G. Gregori, T. Laarmann, K.-H. Meiwes-Broer, A. Przystawik, P. Radcliffe, R. Redmer, H. Reinholz, G. Röpke, R. Thiele, J. Tiggesbäumker, S. Toleikis, N. X. Truong, T. Tschentscher, I. Uschmann, and U. Zastrau, "Thomson scattering from near-solid density plasmas using soft X-ray free electron lasers," High Energy Density Phys. **3**, 120 (2007).

[40]C. Fortmann, R. Thiele, R. R. Fäustlin, T. Bornath, B. Holst, W.-D. Kraeft, V. Schwarz, S. Toleikis, T. Tschentscher, and R. Redmer, "Thomson scattering in

dense plasmas with density and temperature gradients," High Energy Density Phys. **5**, 208 (2009).

[41]D. A. Chapman, D. Kraus, A. L. Kritcher, B. Bachmann, G. W. Collins, R. W. Falcone, J. A. Gaffney, D. O. Gericke, S. H. Glenzer, T. M. Guymer, J. A. Hawreliak, O. L. Landen, S. L. Pape, T. Ma, P. Neumayer, J. Nilsen, A. Pak, R. Redmer, D. C. Swift, J. Vorberger, and T. Döppner, "Simulating x-ray Thomson scattering signals from high-density, millimetre-scale plasmas at the national ignition facility," Phys. Plasmas **21**, 082709 (2014).

[42]D. Kraus, D. A. Chapman, A. L. Kritcher, R. A. Baggott, B. Bachmann, G. W. Collins, S. H. Glenzer, J. A. Hawreliak, D. H. Kalantar, O. L. Landen, T. Ma, S. L. Pape, J. Nilsen, D. C. Swift, P. Neumayer, R. W. Falcone, D. O. Gericke, and T. Döppner, "X-ray scattering measurements on imploding spheres at the National Ignition Facility," Phys. Rev. E **94**, 011202 (2016).

[43]P. M. Kozlowski, B. J. B. Crowley, D. O. Gericke, S. P. Regan, and G. Gregori, "Theory of Thomson scattering in inhomogeneous media," Sci. Rep. **6**, 24283 (2016).

[44]D. H. Froula, J. S. Ross, L. Divol, and S. H. Glenzer, "Thomson-scattering techniques to diagnose local electron and ion temperatures, density, and plasma wave amplitudes in laser produced plasmas (invited)," Rev. Sci. Instrum. **77**, 10–E522 (2006).

[45]J. S. Ross, S. H. Glenzer, J. P. Palastro, B. B. Pollock, D. Price, L. Divol, G. R. Tynan, and D. H. Froula, "Observation of relativistic effects in collective Thomson scattering," Phys. Rev. Lett. **104**, 105001 (2010).

[46]J. P. Palastro, J. S. Ross, B. Pollock, L. Divol, D. H. Froula, and S. H. Glenzer, "Fully relativistic form factor for Thomson scattering," Phys. Rev. E **81**, 036411 (2010).

[47]T. Tschentscher, C. Bressler, J. Grünert, A. Madsen, A. P. Mancuso, M. Meyer, A. Scherz, H. Sinn, and U. Zastrau, "Photon beam transport and scientific instruments at the European XFEL," Appl. Sci. **7**, 592 (2017).

[48]C. Bostedt, S. Boutet, D. M. Fritz, Z. Huang, H. J. Lee, H. T. Lemke, A. Robert, W. F. Schlotter, J. J. Turner, and G. J. Williams, "Linac coherent light source: The first five years," Rev. Mod. Phys. **88**, 015007 (2016).

[49]D. Pile, "First light from SACLA," Nat. Photonics **5**, 456–457 (2011).

[50]M. J. MacDonald, A. M. Saunders, R. W. Falcone, W. Theobald, O. L. Landen, and T. Döppner, "Developing a long-duration Zn K-α source for x-ray scattering experiments," Rev. Sci. Instrum. **89**, 10F109 (2018).

[51]M. J. MacDonald, A. M. Saunders, B. Bachmann, M. Bethkenhagen, L. Divol, M. D. Doyle, L. B. Fletcher, S. H. Glenzer, D. Kraus, O. L. Landen, H. J. LeFevre, S. R. Klein, P. Neumayer, R. Redmer, M. Schörner, N. Whiting, R. W. Falcone, and T. Döppner, "Demonstration of a laser-driven, narrow spectral bandwidth x-ray source for collective x-ray scattering experiments," Phys. Plasmas **28**, 032708 (2021).

[52]G. Giuliani and G. Vignale, *Quantum Theory of the Electron Liquid* (Cambridge University Press, Cambridge, 2008).

[53]T. Döppner, O. L. Landen, H. J. Lee, P. Neumayer, S. P. Regan, and S. H. Glenzer, "Temperature measurement through detailed balance in x-ray Thomson scattering," High Energy Density Phys. **5**, 182–186 (2009).

[54]H. Poole, D. Cao, R. Epstein, I. Golovkin, T. Walton, S. X. Hu, M. Kasim, S. M. Vinko, J. R. Rygg, V. N. Goncharov, G. Gregori, and S. P. Regan, "A case study of using x-ray Thomson scattering to diagnose the in-flight plasma conditions of DT cryogenic implosions," Phys. Plasmas **29**, 072703 (2022).

[55]A. D. Baczewski, L. Shulenburger, M. P. Desjarlais, S. B. Hansen, and R. J. Magyar, "X-ray Thomson scattering in warm dense matter without the Chihara decomposition," Phys. Rev. Lett. **116**, 115004 (2016).

[56]W. Kohn and L. J. Sham, "Self-consistent equations including exchange and correlation effects," Phys. Rev. **140**, A1133–A1138 (1965).

[57]B. Holst, M. French, and R. Redmer, "Electronic transport coefficients from *ab initio* simulations and application to dense liquid hydrogen," Phys. Rev. B **83**, 235120 (2011).

[58]M. Preising and R. Redmer, "Metallization of dense fluid helium from *ab initio* simulations," Phys. Rev. B **102**, 224107 (2020).

[59]K.-U. Plagemann, P. Sperling, R. Thiele, M. P. Desjarlais, C. Fortmann, T. Döppner, H. J. Lee, S. H. Glenzer, and R. Redmer, "Dynamic structure factor in warm dense beryllium," New J. Phys. **14**, 055020 (2012).

[60]C. Mo, Z. Fu, W. Kang, P. Zhang, and X. T. He, "First-principles estimation of electronic temperature from x-ray Thomson scattering spectrum of isochorically heated warm dense matter," Phys. Rev. Lett. **120**, 205002 (2018).

[61]K. Ramakrishna, A. Cangi, T. Dornheim, A. Baczewski, and J. Vorberger, "First-principles modeling of plasmons in aluminum under ambient and extreme conditions," Phys. Rev. B **103**, 125118 (2021).

[62]E. K. U. Gross and W. Kohn, "Local density-functional theory of frequency-dependent linear response," Phys. Rev. Lett. **55**, 2850–2852 (1985).

[63]J. F. Dobson, "Harmonic-potential theorem: Implications for approximate many-body theories," Phys. Rev. Lett. **73**, 2244–2247 (1994).

[64]G. Vignale and W. Kohn, "Current-dependent exchange-correlation potential for dynamical linear response theory," Phys. Rev. Lett. **77**, 2037–2040 (1996).

[65]G. Vignale, C. A. Ullrich, and S. Conti, "Time-dependent density functional theory beyond the adiabatic local density approximation," Phys. Rev. Lett. **79**, 4878–4881 (1997).

[66]J. F. Dobson, M. J. Bünner, and E. K. U. Gross, "Time-dependent density functional theory beyond linear response: An exchange-correlation potential with memory," Phys. Rev. Lett. **79**, 1905–1908 (1997).

[67]N. T. Maitra, K. Burke, and C. Woodward, "Memory in time-dependent density functional theory," Phys. Rev. Lett. **89**, 023002 (2002).

[68]O. Gritsenko and E. J. Baerends, "Asymptotic correction of the exchange–correlation kernel of time-dependent density functional theory for long-range charge-transfer excitations," J. Chem. Phys. **121**, 655–660 (2004).

[69]I. V. Tokatly, "Time-dependent deformation functional theory," Phys. Rev. B **75**, 125105 (2007).

[70]P. Myöhänen, A. Stan, G. Stefanucci, and R. van Leeuwen, "A many-body approach to quantum transport dynamics: Initial correlations and memory effects," Europhys. Lett. **84**, 67001 (2008).

[71]M. Panholzer, M. Gatti, and L. Reining, "Nonlocal and nonadiabatic effects in the charge-density response of solids: A time-dependent density-functional approach," Phys. Rev. Lett. **120**, 166402 (2018).

[72]J. P. F. LeBlanc, K. Chen, K. Haule, N. V. Prokof'ev, and I. S. Tupitsyn, "Dynamic response of the electron gas: Towards the exact exchange-correlation kernel," Phys. Rev. Lett. **129**, 246401 (2022).

[73]N.-H. Kwong and M. Bonitz, "Real-time Kadanoff-Baym approach to plasma oscillations in a correlated electron gas," Phys. Rev. Lett. **84**, 1768 (2000).

[74]J. J. Kas and J. J. Rehr, "Finite temperature Green's function approach for excited state and thermodynamic properties of cool to warm dense matter," Phys. Rev. Lett. **119**, 176403 (2017).

[75]T. Dornheim, S. Groth, J. Vorberger, and M. Bonitz, "Ab initio path integral Monte Carlo results for the dynamic structure factor of correlated electrons: From the electron liquid to warm dense matter," Phys. Rev. Lett. **121**, 255001 (2018).

[76]S. Groth, T. Dornheim, and J. Vorberger, "Ab initio path integral Monte Carlo approach to the static and dynamic density response of the uniform electron gas," Phys. Rev. B **99**, 235122 (2019).

[77]T. Dornheim and J. Vorberger, "Finite-size effects in the reconstruction of dynamic properties from ab initio path integral Monte Carlo simulations," Phys. Rev. E **102**, 063301 (2020).

[78]R. B. Georg, A. N. Halliday, E. A. Schauble, and B. C. Reynolds, "Silicon in the Earth's core," Nature **447**, 1102–1106 (2007).

[79]T. Matsubara, "A new approach to quantum-statistical mechanics," Prog. Theor. Phys. **14**, 351 (1955).

[80]T. Dornheim, J. Vorberger, S. Groth, N. Hoffmann, Z. Moldabekov, and M. Bonitz, "The static local field correction of the warm dense electron gas: An ab initio path integral Monte Carlo study and machine learning representation," J. Chem. Phys. **151**, 194104 (2019).

[81]T. Dornheim, Z. A. Moldabekov, J. Vorberger, and B. Militzer, "Path integral Monte Carlo approach to the structural properties and collective excitations of liquid ^{3}He without fixed nodes," Sci. Rep. **12**, 708 (2022).

[82]M. Jarrell and J. E. Gubernatis, "Bayesian inference and the analytic continuation of imaginary-time quantum Monte Carlo data," Phys. Rep. **269**, 133–195 (1996).

[83]T. Dornheim, S. Groth, and M. Bonitz, "The uniform electron gas at warm dense matter conditions," Phys. Rep. **744**, 1–86 (2018).

[84]C. Fortmann, A. Wierling, and G. Röpke, "Influence of local-field corrections on Thomson scattering in collision-dominated two-component plasmas," Phys. Rev. E **81**, 026405 (2010).

[85]T. R. Preston, K. Appel, E. Brambrink, B. Chen, L. B. Fletcher, C. Fortmann-Grote, S. H. Glenzer, E. Granados, S. Göde, Z. Konôpková, H. J. Lee, H. Marquardt, E. E. McBride, B. Nagler, M. Nakatsutsumi, P. Sperling, B. B. L. Witte, and U. Zastrau, "Measurements of the momentum-dependence of plasmonic excitations in matter around 1 mbar using an x-ray free electron laser," Appl. Phys. Lett. **114**, 014101 (2019).

[86]J. Sheffield, D. Froula, S. H. Glenzer, and N. C. Luhmann, *Plasma Scattering of Electromagnetic Radiation: Theory and Measurement Techniques* (Elsevier Science, 2010).

[87]A. Höll, R. Redmer, G. Röpke, and H. Reinholz, "X-ray Thomson scattering in warm dense matter," Eur. Phys. J. D **29**, 159–162 (2004).

[88]H. Takabe and Y. Kuramitsu, "Recent progress of laboratory astrophysics with intense lasers," High Power Laser Sci. Eng. **9**, e49 (2021).

[89]K. Voigt, M. Zhang, K. Ramakrishna, A. Amouretti, K. Appel, E. Brambrink, V. Cerantola, D. Chekrygina, T. Döppner, R. W. Falcone, K. Falk, L. B. Fletcher, D. O. Gericke, S. Göde, M. Harmand, N. J. Hartley, S. P. Hau-Riege, L. G. Huang, O. S. Humphries, M. Lokamani, M. Makita, A. Pelka, C. Prescher, A. K. Schuster, M. Šmíd, T. Toncian, J. Vorberger, U. Zastrau, T. R. Preston, and D. Kraus, "Demonstration of an x-ray Raman spectroscopy setup to study warm dense carbon at the high energy density instrument of European XFEL," Phys. Plasmas **28**, 082701 (2021).

[90]E. I. Moses, R. N. Boyd, B. A. Remington, C. J. Keane, and R. Al-Ayat, "The national ignition facility: Ushering in a new age for high energy density science," Phys. Plasmas **16**, 041006 (2009).

[91]J. S. Ross, S. H. Glenzer, J. P. Palastro, B. B. Pollock, D. Price, G. R. Tynan, and D. H. Froula, "Thomson scattering measurements in the collective and noncollective regimes in laser produced plasmas (invited)," Rev. Sci. Instrum. **81**, 10D523 (2010).

[92]A. A. Kugler, "Theory of the local field correction in an electron gas," J. Stat. Phys. **12**, 35 (1975).